



Universiteit
Leiden
The Netherlands

The pan-STARRS1 $z > 5.6$ quasar survey. III. The $z \approx 6$ quasar luminosity function

Schindler, J.T.; Bañados, E.; Connor, T.; Decarli, R.; Fan, X.; Farina, E.P.; ... ; Walter, F.

Citation

Schindler, J. T., Bañados, E., Connor, T., Decarli, R., Fan, X., Farina, E. P., ... Walter, F. (2023). The pan-STARRS1 $z > 5.6$ quasar survey. III. The $z \approx 6$ quasar luminosity function. *The Astrophysical Journal*, 943(1). doi:10.3847/1538-4357/aca7ca

Version: Publisher's Version

License: [Creative Commons CC BY 4.0 license](#)

Downloaded from: <https://hdl.handle.net/1887/3716670>

Note: To cite this publication please use the final published version (if applicable).



The Pan-STARRS1 $z > 5.6$ Quasar Survey. III. The $z \approx 6$ Quasar Luminosity Function

Jan-Torge Schindler^{1,2}, Eduardo Bañados¹, Thomas Connor^{3,4}, Roberto Decarli⁵, Xiaohui Fan⁶, Emanuele Paolo Farina⁷, Chiara Mazzucchelli⁸, Riccardo Nanni², Hans-Walter Rix¹, Daniel Stern³, Bram P. Venemans², and Fabian Walter¹

¹ Max Planck Institut für Astronomie, Königstuhl 17, D-69117, Heidelberg, Germany; schindler@strw.leidenuniv.nl

² Leiden Observatory, Leiden University, P.O. Box 9513, 2300 RA Leiden, The Netherlands

³ Jet Propulsion Laboratory, California Institute of Technology, 4800 Oak Grove Drive, Pasadena, CA 91109, USA

⁴ Center for Astrophysics | Harvard & Smithsonian, 60 Garden St., Cambridge, MA 02138, USA

⁵ INAF—Osservatorio di Astrofisica e Scienza dello Spazio, via Gobetti 93/3, I-40129, Bologna, Italy

⁶ Steward Observatory, University of Arizona, 933 N Cherry Ave, Tucson, AZ 85721, USA

⁷ Gemini Observatory, NSF's NOIRLab, 670 N A'ohoku Place, Hilo, HI 96720, USA

⁸ Núcleo de Astronomía, Facultad de Ingeniería y Ciencias, Universidad Diego Portales, Av. Ejército 441, Santiago, 8320000, Chile

Received 2022 August 11; revised 2022 November 15; accepted 2022 November 22; published 2023 January 25

Abstract

We present the $z \approx 6$ type-1 quasar luminosity function (QLF), based on the Pan-STARRS1 (PS1) quasar survey. The PS1 sample includes 125 quasars at $z \approx 5.7\text{--}6.2$, with $-28 \lesssim M_{1450} \lesssim -25$. With the addition of 48 fainter quasars from the SHELLQs survey, we evaluate the $z \approx 6$ QLF over $-28 \lesssim M_{1450} \lesssim -22$. Adopting a double power law with an exponential evolution of the quasar density ($\Phi(z) \propto 10^{k(z-6)}$; $k = -0.7$), we use a maximum likelihood method to model our data. We find a break magnitude of $M^* = -26.38^{+0.63}_{-0.60}$ mag, a faint-end slope of $\alpha = -1.70^{+0.29}_{-0.19}$, and a steep bright-end slope of $\beta = -3.84^{+0.63}_{-1.21}$. Based on our new QLF model, we determine the quasar comoving spatial density at $z \approx 6$ to be $n(M_{1450} < -26) = 1.16^{+0.13}_{-0.12}$ cGpc⁻³. In comparison with the literature, we find the quasar density to evolve with a constant value of $k \approx -0.7$, from $z \approx 7$ to $z \approx 4$. Additionally, we derive an ionizing emissivity of $\epsilon_{912}(z = 6) = 7.23^{+1.65}_{-1.02} \times 10^{22}$ erg s⁻¹ Hz⁻¹ cMpc⁻³, based on the QLF measurement. Given standard assumptions, and the recent measurement of the mean free path by Becker et al. at $z \approx 6$, we calculate an H I photoionizing rate of $\Gamma_{\text{HI}}(z = 6) \approx 6 \times 10^{-16}$ s⁻¹, strongly disfavoring a dominant role of quasars in hydrogen reionization.

Unified Astronomy Thesaurus concepts: Quasars (1319); Supermassive black holes (1663); Reionization (1383); Early universe (435); Luminosity function (942)

1. Introduction

Quasars are rapidly accreting supermassive black holes (SMBHs) at galaxy centers, which shine as the most luminous nontransient light sources in the universe. At low redshift, tight correlations between the SMBH mass and its host galaxy's central properties have called attention to the role of active galactic nuclei (AGNs) in galaxy evolution (see Kormendy & Ho 2013 for a review). Specifically, feedback during bright quasar phases has been identified as a prominent avenue for establishing this relationship (e.g., Di Matteo et al. 2005). In this context, understanding the evolution of quasars has been the subject of increasing attention over recent years, especially their evolution in the early universe. Following the discovery of the first $z \gtrsim 6$ quasars (Fan et al. 2001a), it was quickly realized that SMBHs with masses of $M_{\text{BH}} \approx 10^9 M_{\odot}$ already existed less than 1 Gyr after the Big Bang, placing constraints on their formation. These have been significantly tightened by the discovery of the most distant quasars known today, at $z \approx 7.5$ (Bañados et al. 2018b; Yang et al. 2020; Wang et al. 2021). While single sources have highlighted open questions with regard to SMBH formation (see Inayoshi et al. 2020 for a review), understanding the full demographics at high redshifts will play a key role in addressing them with the quasar

luminosity function (QLF), the main observational statistic for characterizing their population.

At lower redshifts (e.g., Boyle et al. 1988, 2000; Pei 1995), the QLF is most effectively described by a broken double power law (DPL), which has been widely adopted at higher redshifts as a good representation of most quasar samples (e.g., Richards et al. 2006; Shen & Kelly 2012; Ross et al. 2013). In this context, the QLF is described by a break magnitude, a normalization, and two power-law slopes. At $z \approx 6$, the most comprehensive measurement of the QLF has been presented in Matsuoka et al. (2018), using a combined sample built from the Subaru High- z Exploration of Low-Luminosity Quasars (SHELLQs; Matsuoka et al. 2016) project and previous QLF analyses (Jiang et al. 2008, 2016; Willott et al. 2010), with a total of 112 sources, covering a redshift range of $5.7 < z < 6.5$ and luminosities of $-30 \lesssim M_{1450}/\text{mag} \lesssim -22$. Placed in context with the lower-redshift QLF literature (e.g., Richards et al. 2006; Croom et al. 2009; Glikman et al. 2011; Shen & Kelly 2012; Ross et al. 2013; Akiyama et al. 2018; Schindler et al. 2018, 2019; Boutsia et al. 2021; Pan et al. 2022), the recent results underline the (exponential) increase (Schmidt et al. 1995; Fan et al. 2001a) in quasar activity from $z \approx 6$ to its peak at $z = 2\text{--}3$ (Richards et al. 2006; Kulkarni et al. 2019; Shen et al. 2020). The highest-redshift constraint on the QLF at $z \approx 6.7$ (Wang et al. 2019a) indicates an even more rapid decline of quasar activity at $z > 6.5$, with consequences for the upcoming quasars surveys at $z > 8$ (e.g., based on the Euclid mission wide survey; Euclid Collaboration et al. 2019; Scaramella et al. 2022).



Original content from this work may be used under the terms of the Creative Commons Attribution 4.0 licence. Any further distribution of this work must maintain attribution to the author(s) and the title of the work, journal citation and DOI.

Quasars, or AGNs more generally, and star formation are the major sources of UV radiation that drive the reionization of intergalactic hydrogen. The role of quasars in this process, as inferred from the QLF number counts, has been a matter of debate in the literature. Type-1 UV QLFs at $z \approx 5$ (e.g., McGreer et al. 2013, 2018; Yang et al. 2016; Kim et al. 2020; Shin et al. 2020), at $z \approx 6$ (e.g., Jiang et al. 2008, 2016; Kim et al. 2015; Matsuoka et al. 2018), at $z \approx 6.5$ (Wang et al. 2019a), and from the redshift compilation of Kulkarni et al. (2019) provide substantial evidence for a subdominant contribution of quasars to reionization, as compared to star formation, at $z \gtrsim 5$. These results are supported by analysis of the bolometric QLF based on multiwavelength data sets (Shen et al. 2020). On the other hand, Giallongo et al. (2015, 2019) and Grazian et al. (2020) find high quasar number densities for lower-luminosity sources, $-22.5 \leq M_{1450} \leq -18.5$. These studies are based on multiwavelength-selected sources from the Cosmic Assembly Near-IR Deep Extragalactic Legacy Survey GOODS-South, GOODS-North, and Extended Groth Strip (EGS) fields. The analysis in Giallongo et al. (2015, 2019) is largely based on photometric candidates, whereas the study of Grazian et al. (2020) uses spectroscopy for their two sources. Based on these number densities at the faint end, the authors argue that quasars could be the dominant source of ionizing photons at $z \approx 4-6$, which is supported by the analysis of Grazian et al. (2022), based on the QUBRICS quasar survey (Calderone et al. 2019; Boutsia et al. 2020). However, a range of independent deep X-ray studies have reported significantly lower number densities for the faint quasar population (e.g., Weigel et al. 2015; Cappelluti et al. 2016; Vito et al. 2016; Ricci et al. 2017; Parsa et al. 2018), challenging the results of Giallongo et al. (2015, 2019).

In this work, we present a new measurement of the type-1 UV QLF at $z \approx 6$, based on the selection strategy of and discoveries from the Pan-STARRS distant quasar survey (Bañados et al. 2014, 2016, 2022). Our quasar sample includes 125 sources at $z \approx 5.7-6.2$, within a luminosity range of $-28 \lesssim M_{1450} \lesssim -25$, more than doubling the number counts of previous samples in this range (Jiang et al. 2016; Sloan Digital Sky Survey, or SDSS). Combining the new sample with lower-luminosity sources from SHELLQs (Matsuoka et al. 2018), we present the most precise measurement of the type-1 UV QLF at these redshifts to date.

In Section 2, we review the quasar selection of the PS1 distant quasar survey and present the new quasar sample used in this work. Section 3 discusses the resulting quasar selection function and completeness. We present the QLF in Section 4, and we discuss the implications with regard to quasar evolution and reionization in Section 5. Finally, we summarize this work in Section 6. Interested readers can find the mathematical framework for our QLF analysis described in detail in Appendix A, whereas Appendix B expands on the discussion of our quasar model that we use for the completeness calculation. In this work, we adopt a Λ CDM cosmology, with $H_0 = 70 \text{ km s}^{-1} \text{ Mpc}^{-1}$, $\Omega_M = 0.3$, and $\Omega_\Lambda = 0.7$. All magnitudes are reported in the AB photometric system.

2. Data

The foundation of the quasar searches that this work builds upon is the 3π Steradian Survey (Chambers et al. 2016) that was carried out by the Panoramic Survey Telescope and Rapid Response System Telescope #1 (PS1; Kaiser et al. 2002, 2010).

From 2009 to 2015, the PS1 3π survey imaged the sky above a decl. of -30° in the five filter bands g_{P1} , r_{P1} , i_{P1} , z_{P1} , and y_{P1} . The full data releases of the PS1 3π survey are hosted by the Barbara A. Mikulski Archive for Space Telescopes (MAST) at the Space Telescope Science Institute.⁹

2.1. The PS1 3π Steradian Survey PV2 Catalog

The PS1 3π distant quasar survey (Bañados et al. 2014, 2016) based its selection on the internal prereleases of the stacked PS1 3π photometry—in particular, the second internal data release, PV2. According to Bañados et al. (2016, their Section 2.1), the PV2 5σ median limiting magnitudes are $(g_{P1}, r_{P1}, i_{P1}, z_{P1}, y_{P1}) = (23.2, 23.0, 22.7, 22.1, 21.1)$. The quasar selection uses the stacked point-spread function (PSF) magnitude signal to noise ratio (S/N_x) and the (3σ) limiting magnitude ($m_{\text{lim},x}$) of a given band x as selection criteria. These properties are derived from quantities in the PV2 catalog. We briefly describe them here, to provide context for Section 3.1.2, where we discuss the modeling of simulated quasar photometry to assess the selection function completeness. The S/N_x is calculated from the stacked PSF magnitude 1σ uncertainty ($\sigma_{m,x}$) of the same filter band x :

$$S/N_x = \frac{2.5}{\ln 10 \times \sigma_{m,x}}. \quad (1)$$

The 3σ limiting magnitude $m_{\text{lim},x}$ is derived from the band zeropoint ($z_{P,x}$) and the 1σ uncertainty on the stacked PSF fit instrumental flux (PSF_INST_FLUX_SIG):

$$m_{\text{lim},x} = -2.5 \times \log_{10}(3 \times \text{PSF_INST_FLUX_SIG}_x) + z_{P,x}. \quad (2)$$

The PSF_INST_FLUX_SIG is a PV2 catalog property from the internal data release, which is not provided in the public data release on MAST. The band x zeropoint, $z_{P,x}$, only depends on the stacked exposure time (EXPTIME _{x}) in that filter band:

$$z_{P,x} = 25 + 2.5 \times \log_{10}(\text{EXPTIME}_x). \quad (3)$$

All stacked magnitudes are corrected for Galactic extinction using the Schlegel et al. (1998) dust map, with the corrections of Schlafly & Finkbeiner (2011). The quasar photometric selection is conducted on the dereddened stacked magnitudes.

2.2. Quasar Candidate Selection

We follow the quasar selection criteria of Bañados et al. (2016, their Section 2.1.1), focusing on the search for quasars at $5.7 \lesssim z \lesssim 6.2$. The selection criteria are applied to the PS1 PV2 catalog generated from the PS1 image stacks.

For completeness, we briefly describe the selection here. First, we exclude sources that have been flagged as suspicious (see Bañados et al. 2014, Table 6) by the Imaging Processing Pipeline (Magnier et al. 2020a, 2020b). Additionally, we require 85% of the normalized PSF flux in the i_{P1} , z_{P1} , and y_{P1} bands to be located in unmasked pixels ($\text{PSF_QF} > 0.85$). This quality cut leans toward a more complete selection, by including some lower-quality measurements (Magnier et al. 2020b). We will refer to these requirements on the PV2 catalog as our “photometric quality selection” hereafter.

⁹ <https://panstarrs.stsci.edu>

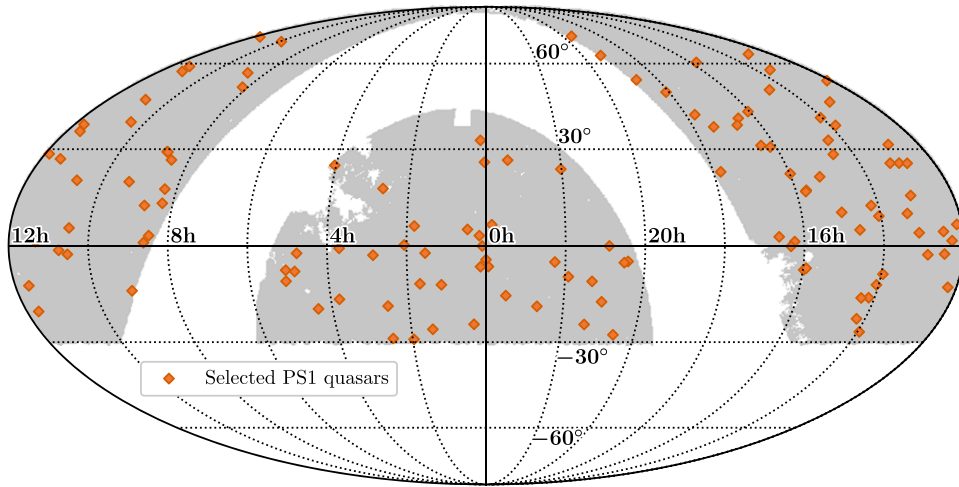


Figure 1. Mollweide projection of the PS1 quasar survey area ($20,803 \text{ deg}^2$) considered for the QLF analysis. The right ascension and decl. are noted in hours and degrees. The regions included in the quasar selection that are based on the PS1 PV2 catalog are shaded in gray, using a HEALPix tessellation with Lvl 10 (12,582,912 HEALPix cells over the entire sky; see Table 2). The M31 mask is included (R.A. $0^{\text{h}} 42^{\text{m}} 44^{\text{s}}$; decl. $+41^{\circ} 16' 9''$). The high-redshift quasars (Section 2.2) are shown as the solid orange diamonds.

The Milky Way plane has traditionally been avoided by quasar surveys using criteria based on Galactic latitudes (e.g., Fan 1999; Jiang et al. 2016). The main reason is because the high source density and stronger Galactic extinction lead to unreliable photometry for extragalactic background sources. Following Bañados et al. (2014), we impose a Galactic latitude limit of $|b| > 20^{\circ}$ and we additionally select only sources with modest degrees of Galactic reddening, as determined from the Schlegel et al. (1998) dust map crossmatched to the PS1 PV2 source catalog, by means of our “extinction selection” criterion:

$$E(B - V) < 0.3. \quad (4)$$

Additionally, we exclude all sources around M31 ($7^{\circ} < \text{R. A.} < 14^{\circ}$; $37^{\circ} < \text{decl.} < 43^{\circ}$), as their inclusion results in a large number of candidates that are most likely stars associated with M31. Figure 1 shows a Mollweide projection of the sky, with the PS1 quasar survey coverage shown in gray. The confirmed high-redshift quasars, as described in this section, are highlighted as orange diamonds. A description of the resulting survey area is provided in Section 3.3, where we discuss the different contributions of the selection criteria to the survey selection function.

Apart from M-, L-, and T-dwarf stars (or brown dwarfs), the main contaminants for high-redshift quasars are low-redshift galaxies, which mostly appear extended under the PS1 observing conditions. The PS1 3π website¹⁰ lists median seeing conditions of $1''.11$, $1''.07$, and $1''.02$ for the i_{P1} , z_{P1} , and y_{P1} filter bands, respectively. To reject the extended sources, we adopt the “morphology criterion,” as discussed in Bañados et al. (2016, their Section 2.1). We keep those sources where the absolute difference between the aperture and PSF magnitudes, $|f_{\text{ext}}|$, is below a value of 0.3 in either the PS1 z or y band:

$$|f_{\text{ext},z}| < 0.3 \text{ OR } |f_{\text{ext},y}| < 0.3. \quad (5)$$

Bañados et al. (2016) tested this criterion against known spectroscopic stars and galaxies in SDSS (DR12; Alam et al. 2015) as well as quasars (SDSS DR10 quasar catalog; Pâris et al. 2014). This criterion removes the majority (92%) of galaxies, while retaining 92% of stars and 97% of quasars.

The focus of this QLF analysis is the redshift range $5.7 \lesssim z \lesssim 6.2$. At these redshifts, quasars can be efficiently differentiated from brown dwarfs by applying color criteria to the PS1 i -, z -, and y -band stacked magnitudes (Bañados et al. 2014). We summarize the “photometric selection” criteria discussed in Bañados et al. (2014) for the $5.7 \lesssim z \lesssim 6.2$ range below:

$$S/N_{z_{\text{P1}}} > 10, \quad (6)$$

$$S/N_{y_{\text{P1}}} > 5, \quad (7)$$

$$(z_{\text{P1}} - y_{\text{P1}}) < 0.5, \quad (8)$$

$$((S/N_{i_{\text{P1}}} \geq 3 \text{ AND } (i_{\text{P1}} - z_{\text{P1}}) > 2.0) \text{ OR } (9)$$

$$(S/N_{i_{\text{P1}}} < 3 \text{ AND } (i_{\text{P1,lim}} - z_{\text{P1}}) > 2.0)), \quad (10)$$

$$(S/N_{r_{\text{P1}}} < 3 \text{ OR } (r_{\text{P1}} - z_{\text{P1}}) > 2.2), \quad (11)$$

$$S/N_{g_{\text{P1}}} < 3. \quad (12)$$

These criteria are applied to the stacked dereddened PS1 magnitudes.

After all the above selection criteria have been applied to the PS1 PV2 photometry, we perform forced photometry on the PS1 stacked and single-epoch images (see Sections 2.2 and 2.3 in Bañados et al. 2014). We remove all sources where the forced photometry is inconsistent with the reported values in the PS1 PV2 catalog. Effectively this removes 80% of the candidates, mainly due to discrepancies in the i_{P1} band (Bañados et al. 2014, their Section 2.2).

After the steps above, which are all automatic, have been completed, this yields a total of 1032 candidates. The PS1 photometry for the z -band and the y -band are taken close in time to each other. Therefore, we visually inspect their stacked and single-epoch images to exclude bright spurious sources (e.g., moving objects) that appear in only one single-epoch z -band/ y -band pair. E.B. and J.T.S. visually inspected all 1032

¹⁰ <https://panstarrs.stsci.edu/>

candidates independently, and assigned a rank from 1 (good photometry) to 4 (inconsistent/erroneous photometry). Sources that are clearly detected in the z band, which have consistent single-epoch measurements and an $i - z$ color in agreement with the catalog, are given rank 1. Sources of rank 2 usually have a fainter detection in the z band, with their stacked y -band measurement being close to the limit of our S/N requirement, such that the single-epoch images are harder to assess. Sources of rank 3 usually have some issues with the data. For example, a clear z -band detection is only visible in one or two epochs. Sources that are given rank 4 show clear data artifacts. The final candidate catalog includes sources for which the summed ranks are 2, 3, or 4. This results in a total of 640 quasar candidates for follow-up observations, 73 sources with summed rank 2, 117 sources with summed rank 3 and 450 sources with summed rank 4. All sources in the final candidate catalog received an individual rank of either 1 or 2 from either E.B. or J.T.S. We exclude a total of 202 sources of summed visual rank 5, as well as 190 sources with an even higher summed visual rank (>5), from further follow-up.

The full quasar selection procedure can be summarized in seven individual steps:

1. Source detection in the PS1 PV2 catalog;
2. Photometric quality selection;
3. Extinction selection and area exclusion;
4. Morphological selection;
5. Photometric selection;
6. Photometry consistency check; and
7. Visual inspection.

Each of these selection steps has an impact on the selection function of the survey, which we discuss in Section 3.3.

2.3. The PS1 High-redshift Quasar Sample

The detailed follow-up strategy, along with descriptions of the photometric and spectroscopic data, is presented in Bañados et al. (2014, 2016, 2022). Of the 640 good quasar candidates, 41 are published quasars in the literature and 274 sources have been photometrically or spectroscopically followed up. The photometric follow-up rejected 79 candidates. These sources were ruled out as good candidates due to their red $y_{P1} - J$ color ($y_{P1} - J > 1$) or if the follow-up photometry did not meet the main selection criteria (Equations (6)–(12)). Our confirmation spectroscopy identified 84 quasars among the 195 observed sources. Due to limited telescope time, 325 quasar candidates have not yet been followed up. We display the full identification statistics in Figure 2. The upper panel shows histograms of the confirmed quasars ($N_{CQ}(y_{P1})$), the rejected candidates ($N_{RC}(y_{P1})$; photometry and spectroscopy), and the total number of candidates. We estimate the identification efficiency, $\text{Eff}_{ID}(y_{P1})$, as the ratio of the confirmed candidates to the total number of identified candidates,

$$\text{Eff}_{ID} = \frac{N_{CQ}}{N_{CQ} + N_{RC}}. \quad (13)$$

We express the identification completeness, $S_{ID}(y_{P1})$, as the number of observed quasars divided by the number of expected quasars, given our efficiency:

$$S_{ID} = \frac{N_{CQ}}{N_{CQ} + \text{Eff}_{ID} \times N_{NoID}}. \quad (14)$$

To calculate a continuous distribution of the completeness and efficiency as a function of y_{P1} , we use a Gaussian kernel density estimate (KDE). A KDE provides a nonparametric representation of the probability density function of a random variable. In comparison to binning, it is smooth and independent of the end points of the bins. For the full sample, we determined the best bandwidth via cross-validation to be around 0.1. We will use this value for all KDE estimates related to the identification completeness. In the follow-up campaigns, the sources were prioritized by visual rank. This leads to a bias in the completeness between samples of different ranks (see Figure 17 in Appendix C). To mitigate the bias, we calculate the expected number of quasars for each rank individually, accounting for the different efficiencies of each sample. We sum the number of expected quasars for each of the three samples (ranks 2, 3, and 4), and then calculate the adjusted identification completeness:

$$S_{ID} = \frac{N_{CQ}}{N_{CQ} + \sum_{r=2}^4 \text{Eff}_{ID,r} \times N_{NoID,r}}. \quad (15)$$

We show the efficiency and the adjusted identification completeness in the bottom panel of Figure 2. The selection efficiency of the full sample is highest at the bright end of the candidate distribution, before declining toward fainter magnitudes. The low number statistics at the faint end (the faintest bin in the top panel) result in an upturn of the efficiency at the faint end. Our sample has been followed up with very high identification completeness at the bright end ($y_{P1} < 20.0$). Toward fainter magnitudes, the completeness declines, with two visible minima at $y_{P1} = 20.75$ and $y_{P1} = 21.3$, where it reaches only 50% and 30%, respectively. At the faint end, $y_{P1} > 21.3$, our follow-up becomes more complete again, and the identification completeness increases.

The full quasar sample used in our QLF analysis consists of the 125 PS1-selected quasars that have been confirmed. Their sky distribution is shown in Figure 1, and we provide a complete list in Appendix D (Table 7). The quasars have redshifts in the range $z = 5.54$ – 6.31 , with a median of 5.88. Their dereddened z -band (y -band) magnitudes are within 18.68–21.53 (19.03–21.47), with a median of 20.36 (20.37).

3. Analysis

The analysis of the QLF requires us to quantify our quasar selection function (see Section 2.2), including a correction for the incomplete spectroscopic follow-up (Section 2.3). In order to realistically evaluate the photometric selection for type-1 quasars, we simulate quasar photometry by taking into account the properties of the PS1 PV2 catalog (e.g., inhomogeneous depth). In particular, to apply the photometric selection criteria from Equations (6)–(12), we need to produce the observed (error-prone) magnitudes, the S/Ns, and the limiting magnitudes. We describe the photometric modeling in Section 3.1, and continue to derive K -correction terms based on these models to estimate the absolute magnitudes with the QLF quasar sample in Section 3.2. The selection function is then evaluated in Section 3.3.

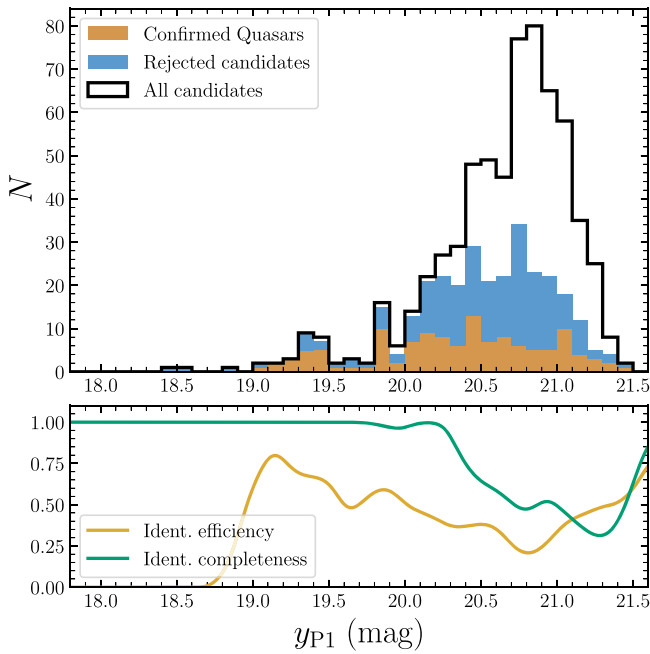


Figure 2. Upper panel: histogram of all the quasar candidates selected for follow-up observations (solid black line) as a function of the dereddened y -band magnitude. Quasars confirmed from the literature or through our observations are shown in orange. Candidates rejected by the observations are shown in light blue, stacked on the confirmed quasars. Lower panel: KDEs of the selection efficiency (yellow) and the adjusted identification completeness (green, Equation (15)), as a function of the dereddened y -band magnitude. The observed completeness and efficiency increase toward the faint end. The KDE extrapolates this beyond the observed magnitude range.

3.1. Modeling PS1 Quasar Photometry

3.1.1. Modeling Quasar Photometry with *simqso*

To build a sample of the simulated quasar photometry, we are using a forked version of the python package *simqso*¹¹ (McGreer et al. 2021), originally presented in McGreer et al. (2013, 2018), which contains updates to the emission line defaults and includes photometric error models for additional surveys. The code constructs artificial quasar spectra from a parametric model of different type-1 quasar spectral components. The parameters are informed by general knowledge of quasar spectra at all redshifts, and they follow the assumption that quasar spectral energy distributions do not evolve with redshift (e.g., Jiang et al. 2006; Shen et al. 2019; Yang et al. 2021). The quasar model is built from a power-law continuum, quasar emission lines, an iron pseudo-continuum component, a dust component, and a component modeling absorption of neutral hydrogen in the intergalactic medium (IGM). Using *simqso*, we have chosen the parameters of the different components to produce a reliable high-redshift quasar model that has been specifically developed for this project.

We construct the continuum from a set of broken power laws ($f_\nu = A \times \nu_\alpha$) that are designed to reproduce the continuum emission of the Selsing et al. (2016) quasar template and the broadband photometry of known SDSS quasars (Schneider et al. 2010; Pâris et al. 2017). The break points and mean power-law slopes are listed in Table 1. For each spectrum, the mean power-law slopes are sampled by drawing values from a Gaussian distribution around the mean slope (α), with a dispersion of $\sigma = 0.3$.

Table 1

Wavelength Break Points and Slopes for the Simulated Quasar Spectra

Break Points in Å	Slope before Break Point (α_ν)
1200	−1.50
2850	−0.50
3645	−0.60
6800	0.00
9000	0.30
30000	0.30
>30000	2.00

We are modeling a total of 65 individual lines (e.g., N V), line complexes (e.g., Si IV+O IV), and individual iron (Fe II and Fe III) multiplets. The majority of these lines are modeled with a single Gaussian, and only five emission lines (Ly α , H α , C IV, C III], and Mg II) are constructed from two Gaussians, with a narrow and a broad component. Correlations between the equivalent widths of some emission lines and the quasar luminosity, i.e., the Baldwin effect (Baldwin 1977), are taken into account. To approximate the emission from the large range of iron transitions seen in the quasar spectra, we include a composite of iron templates. This composite was last updated in *simqso* by Yang et al. (2016), and it uses the Vestergaard & Wilkes (2001) iron template at 1250–2200 Å, the Tsuzuki et al. (2006) iron template at 2200–3500 Å, and the Boroson & Green (1992) iron template at 3500–7500 Å. Following Lyu & Rieke (2017), we add three blackbody components, with temperatures of 1800, 880, and 285 K, to model dust emission. We have adjusted the equivalent width scaling of some emission lines, the amplitude scaling of some regions of the iron template, and the amplitudes of the blackbody dust emission components, in order to fully reproduce the Selsing et al. (2016) quasar template and the optical-to-IR mean quasar colors from the combined sample of the SDSS DR7 (Schneider et al. 2010) and DR12 (Pâris et al. 2017) quasar catalogs. To model the absorption due to neutral hydrogen in the IGM, we use the Ly α forest model of McGreer et al. (2013). We use this model to construct 10,000 different quasar sightlines up to $z = 7$ that are randomly paired with simulated quasars, to produce absorption signatures blueward of the quasar’s Ly α line.

The simulation that we use as the basis for the K -correction to absolute magnitudes and the selection function analysis consists of a uniform grid in absolute magnitude at 1450 Å, $-30 \leq M_{1450} \leq -23$, and redshift, $5.0 \leq z \leq 7.0$, with 56 intervals along the axis of absolute magnitude and 40 intervals along the redshift axis. Each cell is uniformly populated with 88 quasars, for a total of 197,120 quasars. The resulting quasar spectra are then multiplied with the PS1 filter bands to produce synthetic magnitudes.

Recent studies (Yang et al. 2021; Bischetti et al. 2022) have reported an increased broad absorption line (BAL) quasar fraction at $z \gtrsim 6$, compared to lower redshifts. Similar to previous completeness calculations for $z > 6$ QLF measurements (Jiang et al. 2016; Matsuoka et al. 2018; Wang et al. 2019a), our quasar model does not take BAL quasars into account. If our quasar selection were biased against BAL quasars, it would be necessary to account for their different spectral properties in the completeness calculation. Around 40% (six) of the 14 BAL quasars in the Bischetti et al. (2022) sample have weak absorption (balnicity index, or BI < 1000 km s^{−1}), which does not affect the quasar colors beyond the scatter included in our quasar model. On the other hand,

¹¹ <https://github.com/jtschindler/simqso>

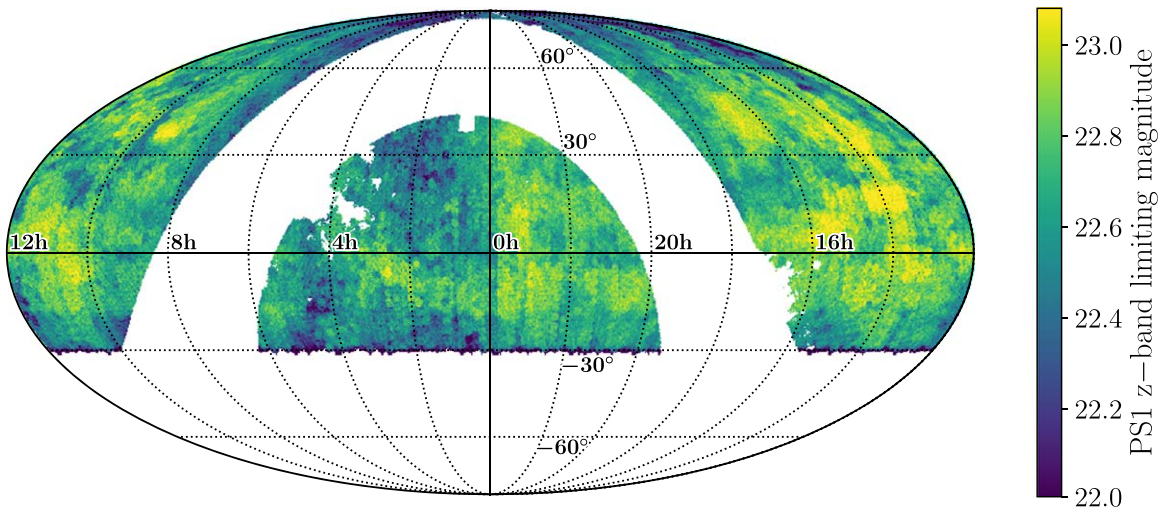


Figure 3. Mollweide projection map of the z -band 3σ limiting magnitude per pixel of the PS1 PV2 survey area (median value per pixel). The map is created from all PV2 sources that obey the quality flags and morphology selection criteria using a HEALPix tessellation with 786,432 pixels (Lvl = 8) over the entire sky. The color range extends from the 1st percentile to the 99th percentile value of all HEALPix pixels, highlighting the strong inhomogeneities in the z band across the survey footprint.

strong broad C IV and Si IV absorption troughs ($BI > 5000 \text{ km s}^{-1}$) will reduce the flux between the C IV and the Ly α lines significantly. At $z > 5.8$, the Si IV line will be in the y_{PS1} band and the C IV line will lie redward of that. Hence, the strongest BAL features will diminish the y_{PS1} -band flux, resulting in a bluer $z_{\text{PS1}} - y_{\text{PS1}}$ color. As a consequence, our color selection, requiring $i_{\text{PS1}} - z_{\text{PS1}} > 2.0$ and $z_{\text{PS1}} - y_{\text{PS1}} < 0.5$, also includes strong BAL quasars naturally, without the need to add them to our quasar model. This inherently high completeness for BAL quasars in our color selection may play a role in the higher BAL fractions discovered at $z > 6$ (Yang et al. 2021; Bischetti et al. 2022).

There is evidence that quasars with weak emission lines (or weak-line quasars, WLQs) could make up $\sim 10\%$ of the population at $z \gtrsim 6$ (e.g., Bañados et al. 2016; Shen et al. 2019), which is higher than what is observed at lower redshifts (Diamond-Stanic et al. 2009). The weaker Ly α and NV emission lines can result in a bluer $i_{\text{PS1}} - z_{\text{PS1}}$ color and a redder $z_{\text{PS1}} - y_{\text{PS1}}$ color for $z > 5.6$ quasars. In the recent literature on $z > 6$ QLFs (e.g., Jiang et al. 2016; Matsuoka et al. 2018; Wang et al. 2019a), a larger fraction of WLQs has not been taken into account, except by Matsuoka et al. (2018), who downscaled the Ly α line of their model spectra to be more inclusive of quasars with weaker emission lines. The spread of the quasar spectral properties covered within the random sampling of *simqso* already covers a significant fraction of the emission line variation. Nonetheless, quasars with very weak lines (e.g., the blue line in Figure 10 of Bañados et al. 2016) are underrepresented in our quasar model (as in all models used for previous QLFs) and may be missed at $z > 6.0$, due to their redder $z_{\text{PS1}} - y_{\text{PS1}}$ (see Figure 16, left panel). This effect introduces a small systematic uncertainty of $< 10\%$ into our QLF analysis, implying that we might be missing $< 10\%$ of quasars at $6.0 \lesssim z \lesssim 6.2$ due to their weak emission lines.

One of the main assumptions for our determination of the selection function is the *simqso* quasar model itself. To test the robustness of this model, we compare it to the quasar model presented by Temple et al. (2021; hereafter, *qsogen*). The Euclid Collaboration et al. (2019) used *qsogen* to predict the quasar yields in the Euclid survey. Both *simqso* and *qsogen* are designed to reproduce the median colors of quasars at $z < 5$.

The $z_{\text{P1}} - y_{\text{P1}}$ quasar colors of both our *simqso* model and *qsogen* agree well with each other. The random sampling of the continuum and emission line properties in the *simqso* model fully encompasses the variation in $z_{\text{P1}} - y_{\text{P1}}$ color introduced by the spread of the emission line properties as parameterized by the *qsogen* *emline_type* parameter. The main difference is the treatment of absorption due to the neutral IGM, which leads to small differences in the $z_{\text{P1}} - y_{\text{P1}}$ color at $z > 5.8$ and larger differences in the $i_{\text{P1}} - z_{\text{P1}}$ color over $z = 5.2 - 6.6$. In comparison to the PS1 quasar colors, the *simqso* model colors provide a more faithful representation of the empirical data points, whereas the default *qsogen* model results in a bluer $i_{\text{P1}} - z_{\text{P1}}$ color. We refer interested readers to the more detailed discussion in Appendix B.

3.1.2. Simulating PS1 Photometric Uncertainties

The *simqso* package allows us to generate synthetic quasar photometry. However, to fully assess the selection function, we need to take the photometric errors into account. For surveys with an approximately homogeneous depth, one can derive simple magnitude error relations from which to sample the photometric error. However, as shown in Figure 3, the PV2 photometric z -band 3σ limiting magnitude (Equation (2)) has strong variations, depending on the sky position. This is also true for all other PS1 bands (e.g., see Figure 19 in Appendix C), and the depth variations do not necessarily correlate with one another across the different filter bands. As a consequence, we cannot define a single magnitude error relation to apply to all simulated quasar photometry. Instead, we adopt a sampling approach, where we randomly associate observed catalog properties with simulated quasars, allowing us to calculate the error properties necessary to evaluate the photometric selection criteria on our simulated sample. Our method is similar in spirit to the approach discussed in Section 3.1 of Yang et al. (2016), which was also adopted for PS1 in Wang et al. (2019b).

The methodology allows us to calculate the stacked PSF magnitude uncertainty (σ_m), which also provides us with the S/N (see Equation (1)) and the 3σ limiting magnitude (m_{lim}) for each simulated quasar. Using σ_m , we can then construct PSF

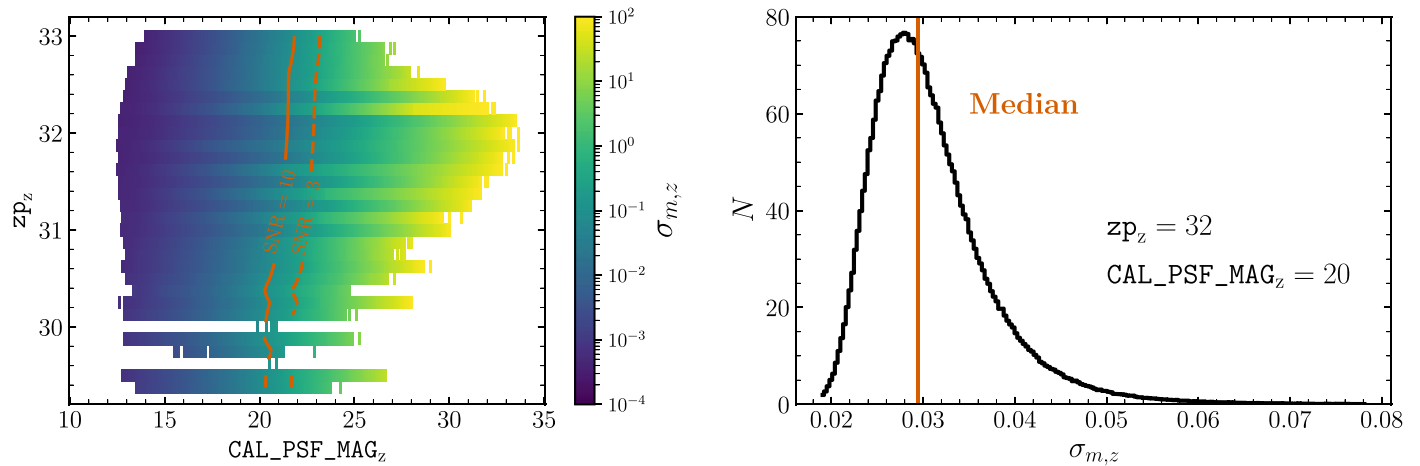


Figure 4. Left: 2D histogram showing the median stacked PSF magnitude error in the z -band $\sigma_{m,z}$ per bin, as a function of the z -band zeropoint zp_z and the stacked PSF magnitude $CAL_PSF_MAG_z$. The lines showing the constant PSF magnitude S/Ns at $S/N = 10$ and $S/N = 3$ highlight that $\sigma_{m,z}$ is dependent on both $CAL_PSF_MAG_z$ and zp_z . Right: histogram of the PSF magnitude error in the z -band $\sigma_{m,z}$ within the 2D bin centered on $zp_z = 32$ and $CAL_PSF_MAG_z = 20$. Even though the 2D histogram (left) shows a clear relation of the median $\sigma_{m,z}$ with both zp_z and $CAL_PSF_MAG_z$, the individual $\sigma_{m,z}$ values within a bin show a significant dispersion around the median.

magnitudes from the synthetic photometry and evaluate the photometric selection function from the simulated quasar sample, including photometric uncertainties.

We begin with the PV2 catalog after applying the quality flags, the extinction selection, and the morphology selection. This guarantees that we are using the properties of point sources that are most similar to our quasar candidates and that also have good-quality photometry within our chosen footprint. In order to sample these properties, we use Hierarchical Equal Area isoLatitude Pixelation (HEALPix;¹² Górski et al. 2005), as implemented in the `healpy` (Zonca et al. 2019) python package, to associate each source in our clean catalog with a small area on the sky, i.e., a HEALPix cell. For this purpose, we subdivide the sky into a map of 196,608 ($Lvl = 7$) cells, of which 100,766 are filled with at least one source. We then sample the source positions as uniformly as possible across the survey footprint, and retrieve their filter band zeropoints and their Galactic reddening values, $E(B - V)$, from the Schlegel et al. (1998) dust map, for each of the 197,120 simulated quasars. Each of the simulated quasars is then randomly associated with the noise properties of a real source in the catalog.

We have used the full cleaned PV2 catalog to investigate the relations between σ_m , the zp , and the stacked PSF magnitude (CAL_PSF_MAG). Figure 4 (left panel) shows a 2D histogram of the median $\sigma_{m,z}$ as a function of zp_z and $CAL_PSF_MAG_z$. The figure shows the expected dependence of $\sigma_{m,z}$ on $CAL_PSF_MAG_z$ and zp_z , which is further highlighted by the slightly diagonal lines of the constant S/N. We note that within each of the 2D bins, a range of $\sigma_{m,z}$ values exists, as depicted in Figure 4 (right). In order to approximate the stacked PSF magnitude error for a simulated quasar, we first use the sampled $E(B - V)$ to redden the synthetic magnitude. The reddened magnitude and the sampled zp then determine the bin in the $\sigma_m(zp, CAL_PSF_MAG)$ 2D histogram (e.g., Figure 4, left panel), from which we randomly draw a σ_m value, given the 1D σ_m distribution in that particular bin (e.g., Figure 4, right panel). This is done for all PS1 filter bands. In rare instances, where the combination of the sampled zp and simulated

CAL_PSF_MAG does not exist in the cleaned PV2 catalog, we adopt the maximum value of the median σ_m in the 2D histogram. This can be the case for synthetic magnitudes in dropout bands (e.g., the PS1 g band) that exceed the observed range of values. From σ_m , we calculate the S/N for each given band using Equation (1). Once we have associated a σ_m with all synthetic quasars and all bands, we perturb the reddened synthetic magnitude, by drawing from a Gaussian distribution with the magnitude as the mean and the associated σ_m as the 1σ uncertainty. In the last step, we subtract the reddening from the perturbed magnitudes to retrieve the appropriate dereddened magnitudes, which are used for the photometric selection function evaluation.

In order to assess the 3σ limiting magnitude m_{lim} (see Equation (2)), we not only require knowledge of zp , but also of the stacked PSF fit instrumental flux uncertainty, $PSF_INST_FLUX_SIG$, at the source position. Similar to σ_m , $PSF_INST_FLUX_SIG$ can also be mapped as a function of zp and CAL_PSF_MAG , as shown in Figure 5. The figure shows the median z -band $PSF_INST_FLUX_SIG$ per bin and depicts it as also being dependent on both zp and CAL_PSF_MAG . In order to associate a $PSF_INST_FLUX_SIG$ value with a simulated quasar, we proceed just as we have done for the magnitude error above. We then calculate the limiting magnitudes for all simulated quasars according to Equation (2).

3.2. K-correction and Absolute Magnitudes

In order to evaluate the QLF as a function of the absolute monochromatic magnitude measured at rest-frame 1450 Å (M_{1450}), we need to be able to calculate M_{1450} from the observed dereddened PS1 stacked PSF magnitudes for our quasar sample. The conversion to rest-frame M_{1450} requires a term that accounts for the changing filter response as the quasar spectrum is being redshifted, the K -correction. We compute a K -correction based on our simulated quasar photometry, as a function of M_{1450} and quasar redshift. As the PS1 z -band cuts out at around 9300 Å, the rest-frame wavelength of 1450 Å falls into the PS1 y band above $z \approx 5.4$. Therefore, we derive the relation between M_{1450} , z , and the dereddened y -band

¹² <http://HEALPix.sf.net/>

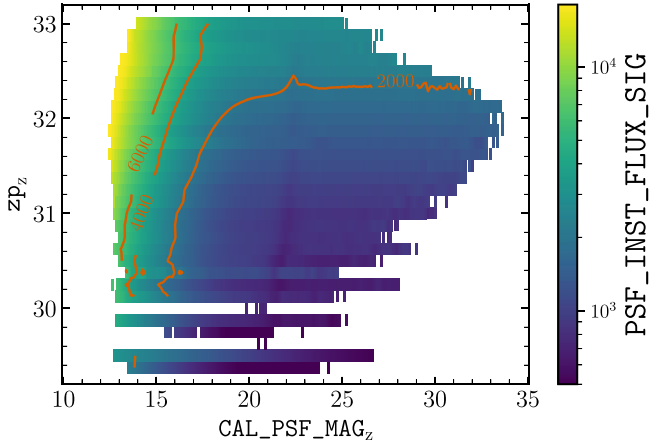


Figure 5. 2D histogram showing the stacked PSF fit instrumental flux uncertainty $\text{PSF_INST_FLUX_SIG}_z$ per bin, as a function of the z -band zeropoint zp_z and stacked PSF magnitude CAL_PSF_MAG_z . The dark red lines show the values of the constant $\text{PSF_INST_FLUX_SIG}_z$ (2000, 4000, and 6000). Similar to the magnitude error in the z -band $\sigma_{m,z}$ (Figure 4), $\text{PSF_INST_FLUX_SIG}_z$ is dependent on both zp_z and CAL_PSF_MAG_z .

magnitude y_{P1} from our grid of simulated quasars. We then retrieve the y_{P1} K -correction factor by interpolation from this relation. Figure 6 shows the luminosity-dependent K -correction factor as a function of redshift for different quasar luminosities. The median absolute deviation (MAD) of the K -correction factor over the entire grid, a measure of its dispersion due to the variety in the different quasar spectra simulated by the code, is $K_{\text{MAD}} = 0.07$ mag. We use this K -correction to calculate M_{1450} from y_{P1} for all the quasars in our QLF sample. The M_{1450} values for each individual quasar are listed in Table 7.

Ideally, one would like to measure the flux at 1450 Å directly from the quasar spectra, to derive M_{1450} . Unfortunately, not all quasars in our sample have the necessary spectral coverage, and therefore we conclude that our photometry-based M_{1450} determination provides a more general approach and allows us to treat all quasars in our sample uniformly.

3.3. The Selection Function

In order to understand the completeness of our quasar selection as a function of absolute magnitude M_{1450} and redshift z , we need to quantify the selection function, following the strategy laid out in Section 2.2. The full survey selection function $S(\mathbf{q})$ can be written as the product of the selection functions for all the independent selection steps. The parameter vector \mathbf{q} contains all the catalog properties that are used in the different selections:

$$S(\mathbf{q}) = S_{\Omega}(\mathbf{q}) \times S_{\text{morph}}(\mathbf{q}) \times S_{\text{phot}}(\mathbf{q}) \times S_{\text{qf}}(\mathbf{q}) \times S_{\text{ID}}(\mathbf{q}). \quad (16)$$

We have separated the selection function for the extinction cut and area exclusion S_{Ω} , the selection function based on morphology S_{morph} (Equation (5)), the photometric selection S_{phot} (Equations (6)–(12)), the quality flag criteria S_{qf} , and the selection function introduced by our incomplete follow-up S_{ID} . Before we present the full survey selection function, we will discuss these individual contributions.

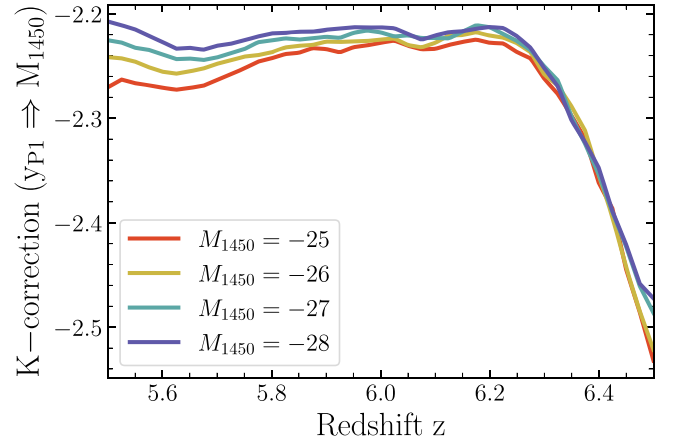


Figure 6. Luminosity-dependent K -correction factor derived from the simulated quasar sample to correct the observed dereddened PS1 stacked PSF y -band magnitude, y_{P1} , to obtain the absolute monochromatic magnitude measured at rest-frame 1450 Å, M_{1450} . The colored lines show the K -correction factor for different luminosities as a function of redshift. The luminosity dependence is most pronounced at $z \approx 5.5$ – 5.8 , where the C IV emission line falls into the PS1 y band.

3.3.1. The Survey Area Estimate and Galactic Extinction

The Galactic extinction $E(B - V)(\alpha, \delta)$ is a function of the R.A. α and decl. δ of the sources. We apply a selection criterion, Equation (4), to construct our sample, which effectively excludes sky regions with high Galactic extinction. Thus, the extinction selection function only reduces the available survey area irrespective of the redshift and luminosity of the sources:

$$S_{\Omega, \text{ext}}(E(B - V), \alpha, \delta) = \begin{cases} 1 & \forall E(B - V)(\alpha, \delta) < 0.3 \\ 0 & \forall E(B - V)(\alpha, \delta) \geq 0.3. \end{cases} \quad (17)$$

We have already noted above (Section 2.2) that, in addition to the extinction cut, the regions close to the Galactic plane ($|b| < 20$ deg),

$$S_{\Omega, \text{gal}}(b) = \begin{cases} 1 & |b| < 20 \text{ deg} \\ 0 & \text{otherwise,} \end{cases} \quad (18)$$

as well as the area around M31,

$$S_{\Omega, \text{M31}}(\alpha, \delta) = \begin{cases} 0 & \forall 7^\circ < \alpha < 14^\circ \text{ AND } 37^\circ < \delta < 43^\circ \\ 1 & \text{otherwise,} \end{cases} \quad (19)$$

are excluded for the final quasar selection as well. The complete area selection function is then a product of the three criteria above:

$$S_{\Omega} = S_{\Omega, \text{ext}} \times S_{\Omega, \text{M31}} \times S_{\Omega, \text{gal}}. \quad (20)$$

To estimate the area included by our selection criteria, we again utilize a HEALPix tessellation of the sky. Our area estimate is based on 328,479,702 sources of the PS1 PV2 catalog, which passed the photometric quality criteria and the morphology selection, and were included in the area defined by the extinction selection and the Galactic plane and M31 exclusion regions. Using HEALPix, we divide the sky into a grid of curvilinear equal-sized quadrilaterals. We calculate the number of HEALPix cells that are populated by at least one

Table 2
Estimates of the Total Survey Area Ω_{total}

Lvl	N_{pix}	$N_{\text{pix, filled}}$	Ω_{pix} (deg ²)	Ω_{total} (deg ²)
6	49,152	25,519	0.83929	21417.93
7	196,608	100,766	0.20982	21143.07
8	786,432	399,766	0.05246	20970.07
9	3,145,728	1,591,062	0.01311	20865.13
10	12,582,912	6,345,413	0.00328	20803.38
11	50,331,648	25,317,657	0.00082	20750.93
12	201,326,592	92,989,674	0.00020	19054.11
13	805,306,368	212,082,285	0.00005	10864.22
14	3,221,225,472	294,119,359	0.00001	3766.67

source, and we sum up the area of all of those cells for a total area estimate. We vary the HEALPix cell sizes to understand the resolution effects on the total estimated area. At the lowest resolution, the sky is represented by 12 HEALpix cells. For the next resolution level, these cells are each divided into four subcells. Hence, the total number of HEALpix cells N_{pix} depends on the resolution level, lvl, following $N_{\text{pix}} = 12 \times 4^{\text{lvl}}$. At too-low resolution levels, the survey area is overestimated, as the coarse cells cannot capture the fine structure of the Galactic extinction map. As we proceed to finer resolutions, the number of HEALpix cells approaches the number of sources for the area estimate. At even higher resolution, the sizes of the HEALpix cells become smaller than the areas between adjacent sources in the survey, and we are effectively undersampling the area. As a result, the survey area estimate decreases rapidly. Table 2 shows the results from the HEALpix analysis. The columns are (1) the HEALpix level Lvl; (2) the total number of pixels N_{pix} per level; (3) the number of filled pixels $N_{\text{pix, filled}}$ per level; (4) the area per pixel Ω_{pix} ; and (5) the total filled area per level Ω_{total} , the effective survey area. The total area estimate drops significantly above lvl = 11, indicating that the HEALPix cell density is approaching the source density and we are beginning to overresolve the area. Thus, we adopt lvl = 10 for our fiducial area estimate, and we use the differences with the adjacent levels to reflect the uncertainties on our estimate. This results in a survey area of $20803.38^{+61.75}_{-54.45}$ deg². This calculated survey area now implicitly takes the extinction selection function into account. We consider the relative uncertainty on the survey area of $\approx 0.3\%$ to be negligible, and it is not propagated further.

3.3.2. Morphology Selection Function

Submillimeter observations indicate that the host galaxies of $z \gtrsim 5.7$ quasars are often compact, with effective (half-light) radii of $R_e \approx 1.11$ kpc (Neeleman et al. 2021). They are effectively unresolved by the PS1 photometry. The selection criterion in Equation (5) is designed to reject extended contaminants from the selection. The quasar completeness was quantified in Bañados et al. (2016, their Section 2.1 and their Figure 3) to be 97%. With the significant detections that we require in the PS1 z and y bands (Equations (6) and (7)), it is reasonable to assume that this value is independent of apparent magnitude and quasar redshift. The host galaxies of quasars only become prevalent at much fainter magnitudes (Matsuoka et al. 2016, their Figure 6) beyond the PS1 detection limit. Therefore, we adopt the value of 97% for the quasar selection

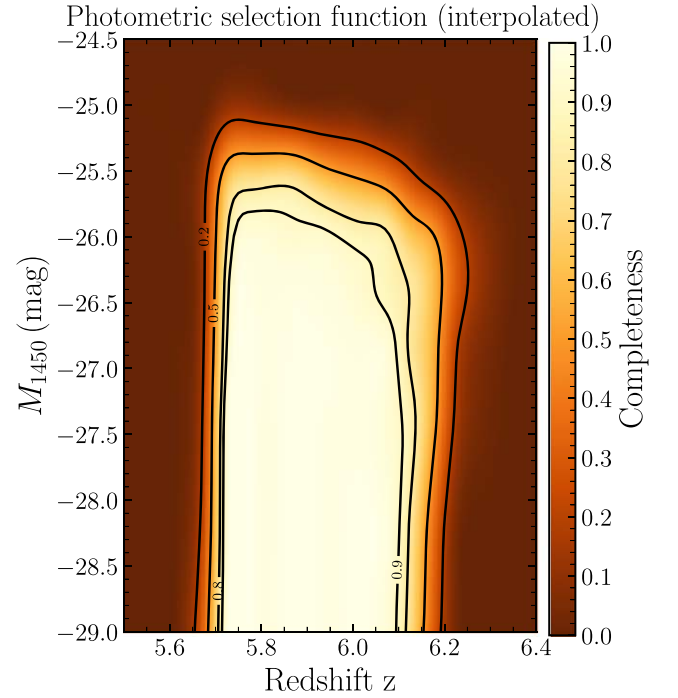


Figure 7. Interpolated photometric selection function evaluated on a redshift (z) and absolute magnitude (M_{1450}) grid of simulated quasars. The black contours are drawn at 20%, 50%, 80%, and 90% completeness, respectively. The high completeness at $5.7 \lesssim z \lesssim 6.2$ directly reflects the color selection criteria listed in Section 2.2. The faint end is limited by the depth of the PS1 survey and the S/N criteria in different filter bands.

completeness:

$$S_{\text{morph}}(f_{\text{ext},z}, f_{\text{ext},y}) = 0.97. \quad (21)$$

Excluding extended sources introduces a bias to our sample against strongly lensed quasars. Multiple images or the foreground lens galaxy could make the lensed quasar appear extended in the imaging.

3.3.3. Photometric Selection Function

The criteria described in Equations (6)–(12) form the core of the PS1 photometry $5.7 \lesssim z \lesssim 6.2$ quasar selection. The photometric selection function is based on the magnitudes and S/Ns in different PS1 filter bands and the limiting i -band magnitude:

$$S_{\text{phot}}(\mathbf{q}) = S_{\text{phot}}(r, i, z, S/N_g, S/N_r, S/N_i, S/N_z, S/N_y, i_{\text{lim,dr}}). \quad (22)$$

We apply the selection criteria to our grid of simulated synthetic quasar photometry (Sections 3.1.1 and 3.1.2) to evaluate its impact as a function of redshift and absolute magnitude. We present the resulting photometric selection function in Figure 7. High-redshift quasars are commonly selected by the strong flux break at the Ly α line, where blueward emission is absorbed by neutral gas in the IGM. The $i_{\text{P1}} - z_{\text{P1}}$ color criterion (Equation (8)) selects quasars with a Ly α break above redshifts of $z \approx 5.6$, and it is responsible for the rise of the selection function at this redshift. The $z_{\text{P1}} - y_{\text{P1}}$ color criterion (Equation (8)) imposes a certain level of continuity between the two filter bands, and thus actively deselects quasars beyond $z \approx 6.3$. The widths of the redshift transition regions depend on the diversity of the quasar spectral

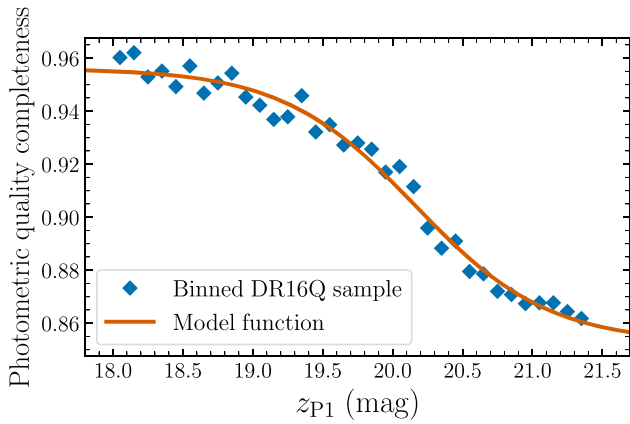


Figure 8. Completeness estimate of our photometric quality selection, as a function of the dereddened PS1 z -band stacked magnitude z_{P1} (blue diamonds). The completeness is calculated in 34 magnitude bins ($z_{P1} = 18\text{--}21.5$, $\Delta z_{P1} = 0.1$) from a sample of 179,945 $z = 2.0\text{--}5.0$ quasars selected from the SDSS DR16 quasar catalog. We approximate the completeness with a hyperbolic tangent function (the solid orange line; Equation (23)) to extrapolate the completeness beyond the measurement limits.

properties and the variations in absorbing neutral hydrogen along the line of sight. The S/N criteria (Equations (6) and (7)) limit the selection in apparent magnitude, resulting in a redshift-dependent absolute magnitude limit. The inhomogeneity of the PS1 depth and the intrinsic scatter of the flux measurements result in a slow decrease with increasing absolute magnitude, rather than a sharp break.

3.3.4. Photometric Quality Selection

We assess the selection function for these photometric quality criteria (see Section 2.2) using two empirical samples of quasars matched to the PS1 PV2 catalog.

As we want to address the completeness of our method, we first build a sample of $z \approx 5.7$, which were discovered from other surveys, but lie within the PS1 footprint. After applying the S/N requirements on the photometry ($S/N_{z_{P1}} > 10$, $S/N_{y_{P1}} > 5$), to ensure an appropriate comparison, we retain 76 sources. We apply the quality criteria and find 72 sources to be included in the photometric quality selection, resulting in a completeness of $\sim 95\%$.

To verify the completeness with a larger sample, we perform an additional test on quasars selected from the SDSS DR16 quasar catalog (Lyke et al. 2020). We require the SDSS quasars to have low extinction ($E(B - V) < 0.3$) and to follow our candidate S/N requirements ($S/N_{z_{P1}} > 10$, $S/N_{y_{P1}} > 5$). Additionally, we only select sources within the redshift range $2 < z < 5$. We exclude quasars from the DR16 quasar catalog at $z > 5$, as the majority of these sources are objects that have been misclassified by the automatic pipeline. Catalog quasars at $z < 2$ are also preemptively excluded, to avoid the complications that arise when the host galaxy starts to be resolved. At that point, the values of PSF_QF and the quality flags will potentially differ significantly from pure point sources. The full sample contains 179,945 SDSS quasars, with 162,770 being retained when applying the photometric quality criteria, resulting in an average completeness of $\sim 90\%$.

We further investigate whether the photometric quality selection function is dependent on the dereddened PS1 z -band magnitude. We thus calculate the completeness in 34 magnitude bins between $z_{P1} = 18$ and 21.5 , with a bin width of $\Delta z_{P1} = 0.1$. The result shows a dependence of the

completeness with z_{P1} (see Figure 8). The quality selection function dependency on the y -band magnitude reflects the correlation between some quality flags (e.g., POORFIT, MOMENT_SN; see Bañados et al. 2014, Table 6) and the lower S/Ns of fainter sources. We model the binned measurements with a hyperbolic tangent,

$$S(z_{P1}) = a \times \tanh(\eta \times (z_{P1} + \phi)) + b, \quad (23)$$

and we use the LMFIT python package (Newville et al. 2014) to retrieve the best-fit parameters via the Levenberg–Marquardt algorithm. The values are $a = 0.052 \pm 0.003$, $b = 0.904 \pm 0.002$, $\eta = -1.049 \pm 0.127$, and $\phi = -20.161 \pm 0.063$. The best-fit model function is shown in Figure 8 as the solid orange line.

We adopt this parameterization of the photometric quality completeness for the calculation of the full selection function. For each point in the space of absolute magnitude M_{1450} and redshift z , we evaluate the photometric quality selection $S(z_{P1})$ by calculating the apparent magnitude $z_{P1}(M_{1450}, z)$ at the point, using the adopted cosmology and a z_{P1} K -correction factor determined analogously to the y_{P1} K -correction (Section 3.2). The photometric quality selection in the space of redshift and absolute magnitude is shown in the left panel of Figure 9. The overall completeness is high, $>85\%$.

3.3.5. Identification Completeness

We further have to take into account that not all of our 640 quasar candidates have been identified through follow-up observations or the literature. We note that spectroscopic follow-up observations were prioritized by the candidate's visual rank. However, no other relevant selection information, e.g., the coordinate range, played a factor in this process. To account for this, we use the weighted identification completeness as a function of y_{P1} , as shown in the bottom panel of Figure 2. Similar to the photometric quality completeness, we evaluate the KDE of the identification completeness $\text{Comp}_{\text{ID}}(y_{P1})$ in the space of redshift (z) and absolute magnitude (M_{1450}), by mapping these properties to the dereddened PS1 y -band magnitude $y_{P1}(M_{1450}, z)$, using the adopted cosmology and the y_{P1} K -correction factor. The right panel of Figure 9 shows the map of the spectroscopic completeness as a function of redshift and absolute magnitude. The low identification completeness ($<80\%$) at the apparent magnitudes $y_{P1} = 20.5\text{--}21.5$ of our follow-up campaigns (Figure 2) is reflected here at absolute magnitudes $M_{1450} \approx -24.9$ to $M_{1450} \approx -26.2$. The completeness rises toward the faint end, equivalent to the behavior in Figure 2, as we have identified many of the faintest candidates.

3.3.6. The Full Survey Selection Function

In order to obtain the full survey selection function, we combine the individual selection functions multiplicatively, according to Equation (16), and present the result in Figure 10. The shape of the selection function is dominated by the photometric selection (see Figure 7). Our incomplete follow-up identification decreases the completeness at the faint end ($M_{1450} = -26.5$ to -25) compared to pure photometric selection. The impact of the photometric quality selection and morphology selection is more subtle, as it decreases the completeness over the full absolute magnitude and redshift

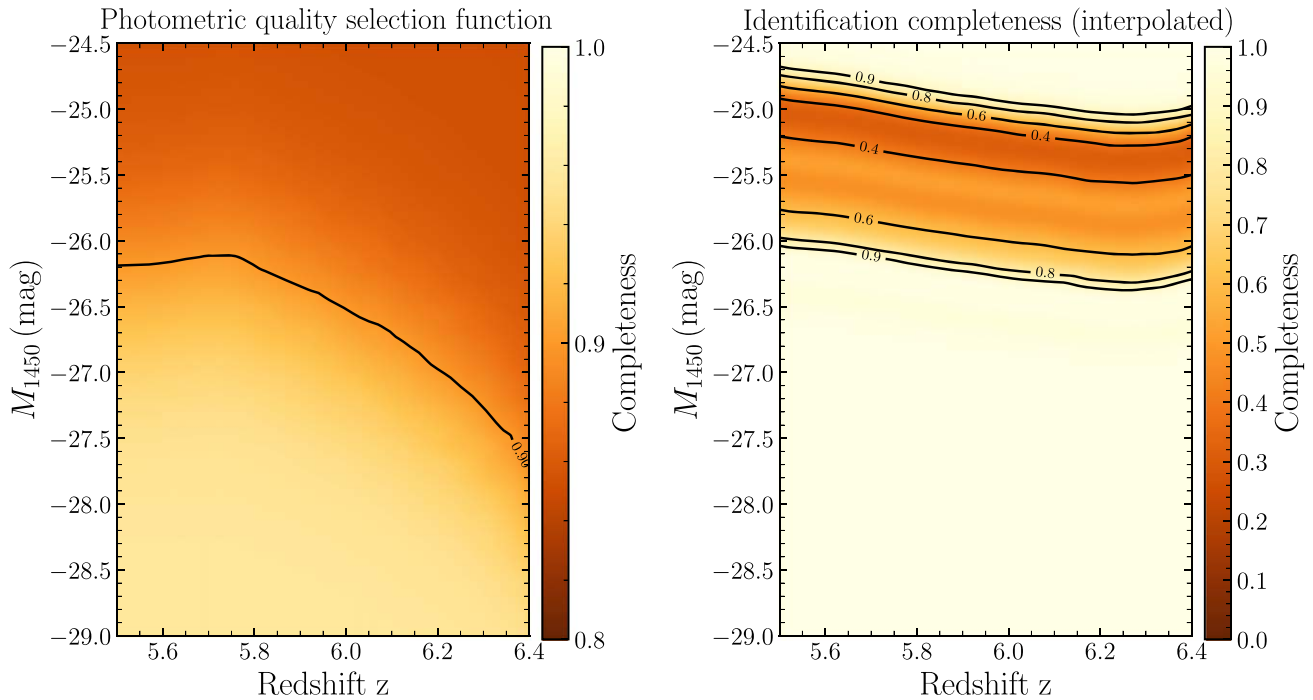


Figure 9. Left: the photometric quality selection function $S(z_{P1}(M_{1450}, z))$ (Equation (23)) as a function of redshift (z) and absolute magnitude (M_{1450}). We retain a relatively high completeness of $>85\%$, as already indicated by the 1D evaluation in Figure 8. In order to emphasize the gradients, we have limited the color scaling of the completeness to the interval $[80\%, 100\%]$. Right: the identification completeness as a function of redshift and absolute magnitude. The low completeness ($<50\%$) at $y_{P1} = 20.5\text{--}21.5$ (see Figure 2) affects the absolute magnitude range from $M_{1450} \approx -24.9$ to $M_{1450} \approx -26.2$, depending on the redshift. Our identification campaigns are largely complete at the faint end (Figure 2), resulting in the rise of the completeness toward the faintest magnitudes. This rise is excluded from our ML fit, for which we use the luminosity range $M_{1450} = -25$ to -29 .

range. We use this selection function to correct for our completeness in the measurements of the QLF.

Figure 10 highlights a few quasars that lie in regions of very low completeness, and it is worthwhile briefly understanding why they have passed our selection strategy. The lowest-redshift quasar of our sample is PSO224.65067+10.21379, at a spectroscopic redshift of $z \approx 5.4$. This source shows strong broad absorption in NV, which effectively removes all Ly α flux, mimicking a Ly α break at $z \geq 5.7$. At the high-redshift end, our sample includes SDSS J1030+0524, at $z = 6.308$. This source, as well as some fainter sources at $z \approx 6.2$ (PSO184.33893+01.52846 and PSO334.01815-05.00488), have especially strong Ly α flux. Due to the resulting blue $z_{P1} - y_{P1}$ color, they are included in our selection (Equation (8)). Finally, our sample includes a number of faint quasars ($M_{1450} \gtrsim -25.5$), with selection probabilities below 20%. This indeed indicates that we expect more than five times as many quasars in this parameter region, in full agreement with previous QLF results (Willott et al. 2010; Matsuoka et al. 2018).

4. Results

In this section, we present our QLF measurement at $z \approx 6$. As the PS1 distant quasar sample only constrains the bright end of the QLF ($M_{1450} < -25$), we combine our sources with 48 quasars from the SHELLQs quasar sample presented in Matsuoka et al. (2018). We adopt the quasar properties based on their Table 1, and we use their selection function (see their Figure 9; the electronic data were provided by Yoshiaki Matsuoka) to correct the SHELLQs sample for incompleteness. We discuss the PS1 QLF binned as a function of absolute magnitude in Section 4.1. Then, in Section 4.2, we fit a DPL to

the combined sample (PS1 + SHELLQs), using a maximum likelihood (ML) approach.

4.1. The Binned QLF

We determine the binned QLF over the redshift interval $5.65 \lesssim z \lesssim 6.25$ in bins of absolute magnitude at 1450 Å. This redshift range includes 121 of the total 125 quasars in our sample. For the calculation of the binned QLF, we implement the $1/V_a$ method (Schmidt 1968; Avni & Bahcall 1980), with the modifications outlined in Page & Carrera (2000). We correct the quasar number counts using the completeness from the full quasar selection function described above (Section 3.3.6). Table 3 summarizes the results. The columns describe (1) the absolute magnitude bin; (2) the median absolute magnitude $\text{med}(M_{1450})$; (3) the median redshift $\text{med}(z)$; (4) the number of quasars per bin; and (5) the uncorrected and (6) corrected binned QLF values (Φ), with uncertainties reflecting the confidence interval for a Poisson distribution that corresponds to 1σ in Gaussian statistics.¹³

The results for our binned PS1 (and SHELLQs) QLF are depicted by the (thin) solid orange diamonds in Figure 11, compared to other binned QLF measurements at $z \sim 6$ from the literature. We compare our results to the binned QLFs determined by Willott et al. (2010; 41 quasars, $5.74 < z < 6.42$, light gray hexagons), Jiang et al. (2016; 47 quasars, $5.7 < z \leq 6.4$, dark gray squares), and Matsuoka et al. (2018; 112 quasars, $5.7 \leq z \leq 6.5$, blue circles). With a total of 121 quasars, the binned PS1 QLF agrees well with the literature data at $z \approx 6$. We note that our sample covers a narrower and

¹³ We approximately calculate this confidence interval as an equivalent to Equations (4) and (5) in Gehrels (1986).

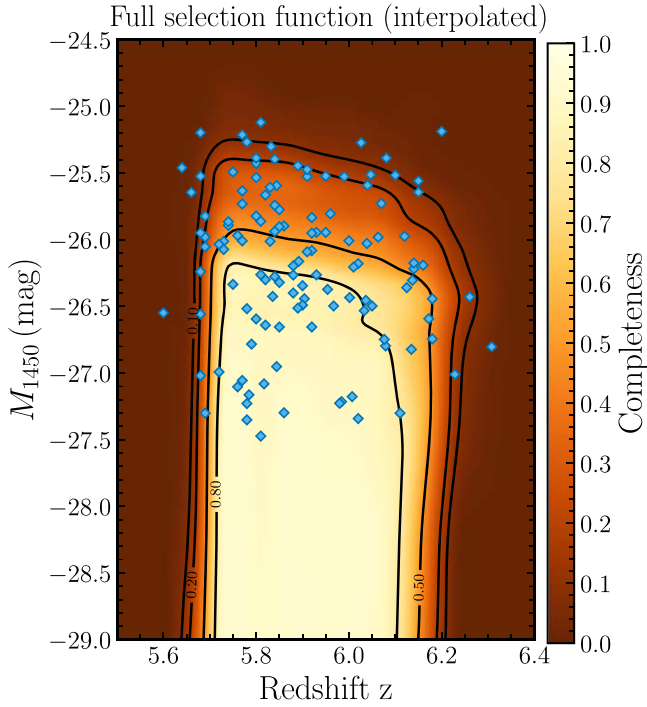


Figure 10. The full PS1 distant quasar survey selection function for the quasar selection focused at $5.7 \lesssim z \lesssim 6.2$. We show the 125 confirmed quasars that make up the QLF sample with blue diamonds. The black contours are drawn at 10%, 20%, 50%, and 80% completeness, respectively.

slightly lower redshift range than previous work in the literature. As a consequence, we miss the bright quasar J0100+2802 at $z = 6.30$ (Wu et al. 2015), and our brightest bin only extends to $M_{1450} = -27.75$. The agreement between our binned values for the SHELLQs sample QLF (thin diamonds) and the values from Matsuoka et al. (2018, blue circles) in the magnitude bins centered at $M_{1450} = -23.25$ and -23.75 is excellent. This demonstrates the consistency of our methods and their implementation, but inadvertently results in the blue circles and orange diamonds completely overlapping in Figure 11. While we only use the SHELLQs data, Matsuoka et al. (2018) derive the binned QLF from a combination of samples, which explains the differences between the thin diamonds and the blue circles.

4.2. ML Estimation of the QLF

The measurement of the binned QLF, while agnostic to its underlying shape, is dependent on the choice of binning, both in luminosity and redshift. With the choice of only one redshift bin, the analysis in the previous section could not account for any redshift evolution of the QLF. Alternatively, we can assume a parametric model for the QLF, including redshift evolution, and constrain the model QLF $\Phi(M, z|\Theta_{\text{QLF}})$ and its parameters Θ_{QLF} by Markov Chain Monte Carlo (MCMC) sampling from the probability of the model QLF, given the observed quasar sample $N(M, z)$, $P_{\text{QLF}} \equiv P(N(M, z)|\Phi(M, z|\Theta_{\text{QLF}}))$. We follow Marshall et al. (1983) in deriving the logarithmic probability $\ln(P_{\text{QLF}})$. We present the full derivation of the logarithmic probability for a luminosity function model $\Phi(M, z|\Theta_{\text{QLF}})$, with a selection function $S(q)$, in Appendix A. The logarithmic probability $\ln(P_{\text{QLF}})$ can then be approximated

as (see also Equation (A16))

$$\ln(P_{\text{QLF}}) \propto \sum_{j=1}^{N(M,z)} \ln[\Phi(M_j, z_j|\Theta_{\text{QLF}})S_j(q(M_j, z_j))] - \Lambda(M, z), \quad (24)$$

where $\Lambda(M, z)$ is the quasar incidence rate, as given by Equation (A6). Given a large enough dynamic range in luminosity, the QLF at low redshift is well approximated by a broken DPL (e.g., Boyle et al. 2000),

$$\Phi(M, z) = \frac{\Phi^*(z)}{10^{0.4(\alpha+1)(M-M^*)} + 10^{0.4(\beta+1)(M-M^*)}}, \quad (25)$$

defined by the normalization Φ^* , the break magnitude M^* , and the two power-law slopes α and β . By convention, α is most commonly chosen as the faint-end slope, with β describing the bright-end slope. Generally, all four parameters could evolve with redshift (see, e.g., Kulkarni et al. 2019). Our sample only spans a narrow redshift interval, therefore we only adopt a redshift evolution for the normalization in the form of

$$\log(\Phi^*(z)) = \log(\Phi^*(z = 6)) + k \times (z - 6). \quad (26)$$

The parameter k describes the exponential evolution of the quasar density with redshift. We implement the luminosity function model and the calculation of the logarithmic probability, then use the python package `emcee` (Foreman-Mackey et al. 2013) for efficient MCMC sampling of the parameter space. For each model fit, we run `emcee` with 10,000 steps and 50 walkers, for a total of 500,000 samples. After discarding the first 1000 steps for each walker, we retrieve the full flat chain of 450,000 realizations. For our fit to the PS1 sample, we use a luminosity range of $M_{1450} = -29$ to -25 and a redshift range of $z = 5.65$ to 6.25 , which includes 121 quasars. The SHELLQs sample covers data with lower luminosities, $M_{1450} = -27.8$ to -22 , and a larger redshift range, $z = 5.705$ to 6.495 .

Our fiducial model fits the four main DPL parameters, based on the combined PS1 and SHELLQs quasar samples, while assuming a fixed value for the normalization evolution $k = -0.7$. Our choice is motivated by previous QLF measurements at $z \approx 5-7$ (McGreer et al. 2013; Jiang et al. 2016; Wang et al. 2019b; Pan et al. 2022), and makes the results easily comparable to those of Matsuoka et al. (2018), where the same value for k was used. The covariance matrix of the fit parameters is shown in Figure 18. We note that the SHELLQs quasar sample covers a larger redshift range than ours. This is taken into account in our ML formulation, given our assumption of the redshift evolution. Figure 11 shows our fiducial QLF model compared to the binned QLF values and literature data at $z = 6$ (Willott et al. 2010; Jiang et al. 2016; Matsuoka et al. 2018). The shaded regions include the 16th to 84th percentile range of all 450,000 realizations (our posterior). The fit results are provided in Table 4, along with their uncertainties (the 16th to 84th percentile range). The first two columns of the table specify the model and the data used in the fit. Table 5 summarizes selected QLF studies from the literature for comparison. The figure highlights two characteristics of our new QLF DPL fit. The bright-end slope is significantly steeper than previous measurements, and the overall number densities

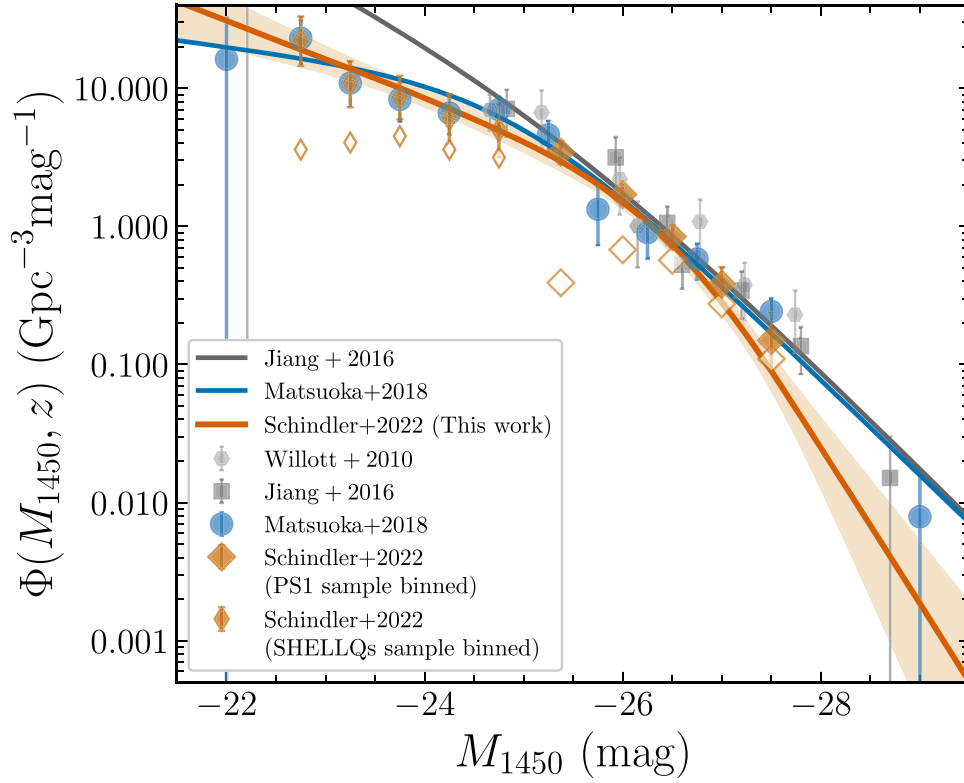


Figure 11. The $z \sim 6$ QLF from the combined SHELLQs and PS1 distant quasar survey samples (orange). We show the binned QLF measurements from the SHELLQs sample and from the PS1 distant quasar survey as the thin and broad orange diamonds, respectively. The open symbols depict the binned QLF when the selection function is not taken into account. The light gray hexagons, gray squares, and blue circles denote the binned measurements from the studies of Willott et al. (2010), Jiang et al. (2016), and Matsuoka et al. (2018). The solid orange line is the median value of the full posterior from our ML MCMC DPL fit, with fixed density evolution ($k = -0.7$), where the shaded region highlights the 16th to 84th percentile uncertainty. For comparison, we also show the best-fit DPL models for the Jiang et al. (2016) QLF and the Matsuoka et al. (2018) QLF, as the blue and gray solid lines, respectively. All the parametric QLF fits have been evaluated at $z = 6.0$.

Table 3
The Binned PS1 Distant Quasar Survey QLF at $5.7 \leq z \leq 6.2$

M_{1450} Bin (mag)	med(M_{1450}) (mag)	med(z)	N	Φ (Uncorr.) ($\text{Gpc}^{-3} \text{mag}^{-1}$)	Φ ($\text{Gpc}^{-3} \text{mag}^{-1}$)
-27.50 ± 0.25	-27.32	5.83	6	0.110	$0.149^{+0.089}_{-0.059}$
-27.00 ± 0.25	-27.06	5.82	15	0.275	$0.381^{+0.126}_{-0.097}$
-26.50 ± 0.25	-26.44	5.90	31	0.567	$0.843^{+0.180}_{-0.151}$
-26.00 ± 0.25	-25.98	5.86	37	0.677	$1.700^{+0.328}_{-0.278}$
-25.38 ± 0.38	-25.52	5.84	32	0.391	$3.433^{+0.721}_{-0.604}$

are lower, with the orange curve lying beneath the blue and gray curves for the majority of the magnitude range.

To test the robustness of our fiducial QLF fit results, we explore four variations on the model. The first variation mimics our fiducial model, but allows k to vary during the fit. The results are in good agreement with our fiducial model. However, the best-fit value for k is -0.20 ± 0.2 , in tension with our assumption of $k = -0.7$. We will continue to discuss this inconsistency below. In a second variation, we fit a single power law (SPL) with $k = -0.7$ to the PS1 quasar sample, without the additional SHELLQs data. The PS1 data alone can be well described by this SPL, with a slope of $\alpha = -2.81$ and a normalization of $\log \Phi^*(z = 6) = -8.85$. Figure 12 shows the SPL fit (yellow) against our DPL fiducial model (gray). The third variation uses our fiducial model, but only includes PS1 quasars with $M_{1450} \leq -26$, in addition to the SHELLQs sample. It is designed to exclude the region of lower spectroscopic completeness (see the right panel in Figure 9), to understand its influence on the fit results. All fit parameters change slightly

within the uncertainties of the fiducial model. Comparing this variation (teal) to the fiducial model (gray) in Figure 12 underlines that the differences over the constrained magnitude range are negligible. We conclude that the magnitude range of low spectroscopic completeness has a minor influence on our fiducial results. Due to the restricted redshift range of the PS1 quasar sample, we miss two bright quasars included in Jiang et al. (2016) and Matsuoka et al. (2018). These are J1148+5251, at $z = 6.42$, with $M_{1450} = -27.8$, and J0100+2802, at $z = 6.30$, with $M_{1450} = -29.1$. As a test, we artificially add these two sources, with a nominal redshift of $z = 6$, to our quasar sample, then fit it again with our fiducial model. We denote this variation as the bright-end test in Figure 12 and Table 4. The artificial inclusion of these two bright sources significantly changes all the QLF parameters, which is reflected in the different shape of this variation (orange) as compared to our fiducial model (gray) in Figure 12. Most notably, the bright-end slope changes to $\beta = -3.12$ and the break is now 0.8 mag fainter. This test highlights the strong influence that individual

Table 4
PS1 QLF Parameter Values as Constrained by the ML Fit

Model	Data	$\log \Phi^*(z=6)$ ($\text{Mpc}^{-3} \text{mag}^{-1}$)	M^* (mag)	α	β	k
DPL	PS1 + SHELLQs	$-8.75^{+0.47}_{-0.41}$	$-26.38^{+0.79}_{-0.60}$	$-1.70^{+0.29}_{-0.19}$	$-3.84^{+0.63}_{-1.21}$	-0.70^a
DPL	PS1 + SHELLQs	$-8.74^{+0.38}_{-0.35}$	$-26.45^{+0.64}_{-0.51}$	$-1.66^{+0.24}_{-0.18}$	$-3.95^{+0.62}_{-1.12}$	$-0.20^{+0.20}_{-0.20}$
SPL	PS1	$-8.85^{+0.04}_{-0.04}$	-26.00^a	$-2.81^{+0.14}_{-0.14}$		-0.70^a
DPL	PS1 ($M_{1450} < -26$) + SHELLQs	$-9.09^{+0.72}_{-0.34}$	$-26.84^{+1.09}_{-0.45}$	$-1.85^{+0.36}_{-0.15}$	$-4.41^{+1.09}_{-1.77}$	-0.70^a
DPL	PS1 + SHELLQs DPL; bright-end test	$-8.28^{+0.39}_{-0.44}$	$-25.57^{+0.80}_{-0.77}$	$-1.45^{+0.38}_{-0.26}$	$-3.12^{+0.32}_{-0.45}$	-0.70^a

Note.

^a Parameters held fixed in the QLF analysis.

Table 5
Selected Literature QLF Measurements at $z > 4.5$

Reference	Redshift Range	Model	$\log \Phi^*(z=6)$ ($\text{Mpc}^{-3} \text{mag}^{-1}$)	M^* (mag)	α	β	k
Willott et al. (2010)	$5.74 < z < 6.42$	DPL	-7.94	-25.13	-1.5^a	-2.81	-0.47^a
Jiang et al. (2016)	$5.7 < z \leq 6.4$	DPL	-8.00	$-25.2^{+1.2}_{-3.8}$	$-1.9^{+0.44}_{-0.58}$	-2.8^a	-0.70^a
Matsuoka et al. (2018)	$5.7 \leq z \leq 6.5$	DPL	$-7.96^{+0.32}_{-0.42}$	$-24.9^{+0.75}_{-0.9}$	$-1.23^{+0.44}_{-0.34}$	$-2.73^{+0.23}_{-0.31}$	-0.70^a
Yang et al. (2016)	$4.7 \leq z \leq 5.4$	DPL	$-8.82^{+0.15}_{-0.15}$	$-26.98^{+0.23}_{-0.23}$	-2.03^a	$-3.58^{+0.24}_{-0.24}$	-0.47^a
McGreer et al. (2018)	$4.7 \leq z \leq 5.4$	DPL	$-8.97^{+0.15}_{-0.18}$	$-27.47^{+0.22}_{-0.26}$	$-1.97^{+0.09}_{-0.09}$	-4.0^a	-0.47^a
Wang et al. (2019b)	$6.45 \leq z \leq 7.05$	DPL	$-8.49^{+0.10}_{-0.14}$	-25.2^a	-1.9^a	$-2.54^{+0.29}_{-0.29}$	-0.78^a

Note.

^a Parameters held fixed in the QLF analysis.

sources at the extreme bright end can have on the QLF measurement.

With the conclusions from the different fit variations in mind, we now discuss our fiducial fit results in the context of the current literature. Our QLF model favors a break magnitude of $M_{1450} = -26.38$. This value is brighter than previous work at $z \approx 6$ (Willott et al. 2010; Jiang et al. 2016; Matsuoka et al. 2018), but also fainter than work at $z \approx 5$ (Yang et al. 2016; McGreer et al. 2018). It is also significantly fainter than the study of Kulkarni et al. (2019), which models the QLF from $z = 0$ to 6 and fits a break magnitude of $M_{1450} \approx -29$ at $z = 6$, effectively constraining only the faint-end slope with the data at $z = 6$. The differences between the results of Jiang et al. (2016) and Matsuoka et al. (2018) are at least in part due to the inclusion of bright quasars at $z > 6.25$ in these samples, as our bright-end test (Table 4, final row) highlights.

Allowing for k to vary, or excluding the fainter PS1 sample data with high spectroscopic incompleteness from our fit (see the second and fourth rows of Table 4), does not change our best-fit break magnitude significantly, given its uncertainties. Rather, it seems to be a robust result, given the combined PS1 + SHELLQs quasar sample (see also Figure 18).

The break magnitude M_{1450} and density normalization $\Phi^*(z=6)$ values are highly covariant in a broken DPL (Figure 18). As a natural consequence of our brighter break magnitude, we measure a lower value of $\Phi^*(z=6)$ than the previous studies at $z = 6$. Taking this covariance into account, our best-fit QLF model agrees well with previous determinations, especially.

Our fiducial best fit returns a bright-end slope with a relatively steep value of $\beta = -3.84$, significantly steeper than the literature data at $z = 6$ ($\beta \approx -2.8$; Willott et al. 2010; Jiang et al. 2016; Matsuoka et al. 2018). The exception is the study of

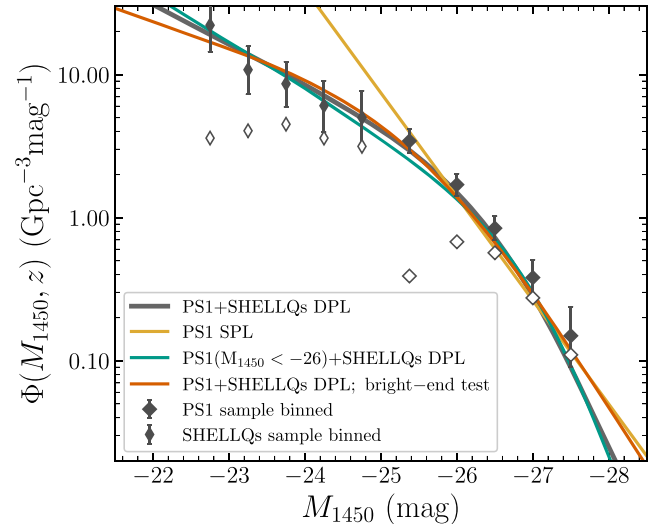


Figure 12. We compare our fiducial QLF DPL fit (dark gray) to an SPL fit to the PS1 sample (yellow) and a DPL fit to the combined PS1 + SHELLQs sample, with the PS1 sample restricted to $M_{1450} \leq -26$ (teal), excluding the range of low spectroscopic completeness. The binned QLF is shown in dark gray, with the open symbols denoting the values not corrected for completeness. The shading indicates the 16th to 84th percentile region of the posteriors.

Kulkarni et al. (2019). Following their global QLF fit, they find a very steep bright-end slope of $\beta = -5.05^{+0.76}_{-1.18}$. However, their work does not yet include the faint SHELLQs quasars at $z \gtrsim 6$. In consequence, they derive an extremely bright best-fit break magnitude at $z = 6$, $M^* \approx -29$, such that the data that they use only constrain the faint-end slope at this redshift. We emphasize that the PS1 quasar sample that determines β covers a narrower redshift range. Therefore, our samples do not

include some very luminous quasars at $z > 6.25$, e.g., J1148+J1148+5251 or J0100+2802. Artificially including these sources in our sample with an assumed redshift of $z=6$ changes the best-fit model results significantly (Table 4, final row). We conclude that these few sources at very bright magnitudes are the main driver of the differences between our fiducial measurements and the studies of Jiang et al. (2016) and Matsuoka et al. (2018). On the other hand, a steep bright-end slope is not uncommon. In fact, at $z \lesssim 5$, a range of studies (e.g., Richards et al. 2006; McGreer et al. 2013; Yang et al. 2016) find a bright-end slope of $\beta \lesssim -3$, with some studies reporting an even steeper slope of $\beta \approx -4$ (Schindler et al. 2019; Boutsia et al. 2021; Pan et al. 2022). Viewed in this context, our results at $z \approx 6$ indicate that the bright-end slope is generally steep ($\beta \approx -4$), and does not evolve significantly with redshift.

The faint-end slope measurement of our ML fit is largely determined by the SHELLQs quasar sample. Our best-fit value of $\alpha = -1.70$ lies between the value of $\alpha = -1.23$ measured by Matsuoka et al. (2018) and the previous determination of $\alpha = -1.9$ by Jiang et al. (2016). The addition of the SHELLQs sample to our fit explains the flatter slope compared to Jiang et al. (2016), as data at these faint luminosities were not available at the time. The 2σ differences with the results of Matsuoka et al. (2018) are mostly driven by the influence of bright sources (Table 4, final row) on the QLF results, which are present in their sample, but not included in ours. These sources significantly affect the resulting break magnitude, which is covariant with the faint-end slope (see Figure 18). Additionally, the QLF of Matsuoka et al. (2018) includes data from Willott et al. (2010) that are not present in our analysis.

Our fiducial QLF fit assumes an exponential density evolution with $k \approx -0.7$. As a test, we remove this assumption and allow k to vary, resulting in a best-fit value of $k = -0.20 \pm 0.2$. This value is in tension with our assumption, but does this mean that our assumption of $k \approx -0.7$ is not justified? We have based the assumption on literature data, and the following discussion of the quasar density redshift evolution in Section 5.1 strongly supports our assumed value of k for the fiducial fit. Hence, we conclude that the redshift range, which is limited by our sample selection, is not large enough to probe the quasar density evolution sufficiently.

5. Discussion

5.1. Evolution of the $M_{1450} < -26$ Quasar Density

The bright-end quasar density $n(M_{1450} < -26)$ has been known to increase from $z \approx 5$ to $z \approx 2$ (Schmidt et al. 1995). Fan et al. (2001a) modeled the quasar density up to $z \approx 6$, with $n(M_{1450} < -26) \propto 10^{k(z-z_{\text{ref}})}$, finding a value of $k = -0.47$. McGreer et al. (2013) and Jiang et al. (2016) reported an even steeper increase in the luminous quasar density, with $k = -0.7$, the factor assumed in our ML analysis above. From $z \approx 7$ to $z \approx 6$, the quasar density is reported to increase even more steeply, with $k = -0.78$ (Wang et al. 2019b). This finding is supported by quasar searches from the VIKING survey (B. Venemans 2022, private communication) that go beyond the first discoveries (Venemans et al. 2013). Going backward in cosmic time, this seemingly accelerating decrease in quasar density has important consequences for the predicted number of discoverable quasars at even higher redshifts, $z > 8$. In Figure 13, we compare the QLFs of Wang et al. (2019b) at

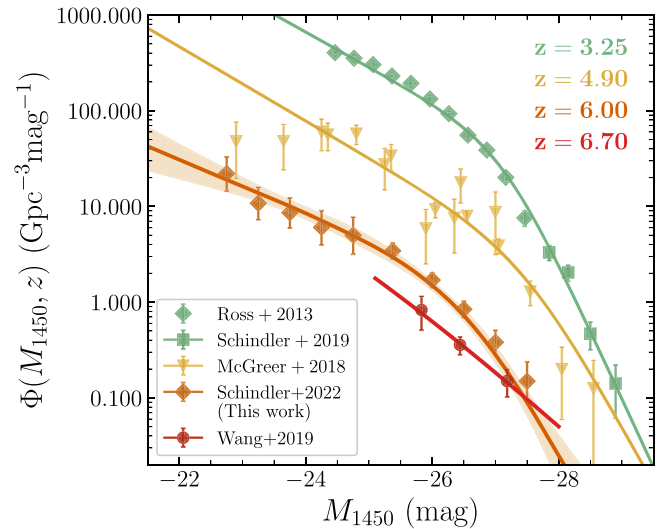


Figure 13. Redshift evolution of the QLF from $z \approx 3$ to 7, colored by redshift. The solid symbols show the binned QLFs at these redshifts, from different studies in the literature (Ross et al. 2013; McGreer et al. 2018; Schindler et al. 2019; Wang et al. 2019b). This comparison visualizes the strong decline in quasar number densities from redshift $z \approx 3$ to 7.

$z = 6.7$, of McGreer et al. (2018) at $z = 4.9$, and of Schindler et al. (2019) at $z = 3.25$ with our results at $z = 6.0$. The figure shows the rise in quasar number counts from $z = 6.7$ to 3.25.

To determine the quasar density at the bright end, we integrate our best-fit QLF at $z = 5.85$ down to $M_{1450} = -26$. This results in a value of $n(M_{1450} < -26) = 1.16^{+0.13}_{-0.12} \text{ cGpc}^{-3}$, which is in line with the other measurements at $z \approx 6$ (Willott et al. 2010; Jiang et al. 2016; Matsuoka et al. 2016). We choose a redshift of $z = 5.85$, close to the median redshift of the PS1 quasar sample (see Table 3), which determines this magnitude range of the QLF. We show our result in comparison to values from the literature in Figure 14. We include a range of studies that provide a significant reevaluation of the QLF at $z = 3-5$ (Akiyama et al. 2018; Schindler et al. 2018, 2019; Giallongo et al. 2019; Boutsia et al. 2021; Onken et al. 2022), compared to the first results from SDSS (Richards et al. 2006; Shen & Kelly 2012; Ross et al. 2013). We also show the redshift evolution from integrating the quasar density from the QLFs of Richards et al. (2006; $z = 0.3-5$) and Kulkarni et al. (2019; $z = 0.3-6$), as the gray dotted and dotted-dashed lines. We note that Niida et al. (2020) and Kim et al. (2020) also provide updated measurements on the $z \approx 5$ QLF. Their integrated quasar densities are consistent with that of McGreer et al. (2018), and so we do not display them in Figure 14, for the sake of its readability.

The quasar densities from the studies of Boutsia et al. (2021) and Giallongo et al. (2019) stand out in Figure 14, reporting significantly larger values than the remaining literature. In the work of Boutsia et al. (2021) the $M_{1450} \sim -26$ luminosities at $z \approx 4$ are largely dominated by the assumed Fontanot et al. (2007) QLF, with densities larger than reported in Richards et al. (2006), as adopted in Schindler et al. (2019) and Akiyama et al. (2018). The adoption of the binned Fontanot et al. (2007) QLF values for their analysis thus explains the large number densities compared to other studies at the same redshift. The analysis of Giallongo et al. (2019), on the other hand, relies on photometric redshifts and does not include data that constrain their QLF model at $M_{1450} \sim -27$ to -25 , the critical range for determining $n(M_{1450} < -26)$. Therefore,

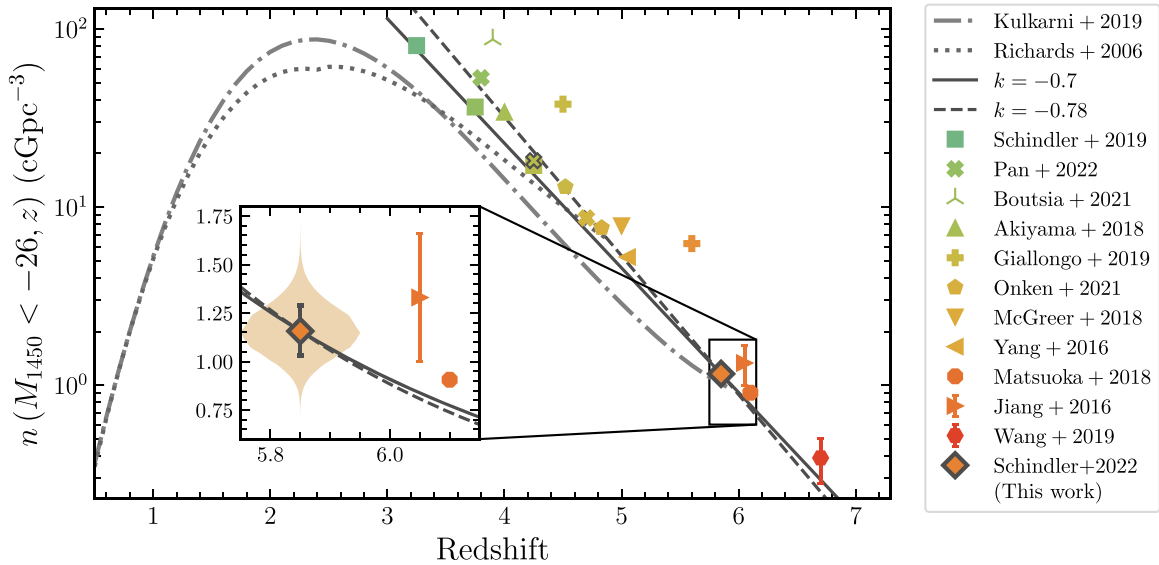


Figure 14. The density of luminous quasars $n(M_{1450} < -26)$ as a function of redshift. Our result, integrating our QLF DPL (the first row in Table 4) at $z = 5.85$, is shown as an orange diamond. The uncertainties (gray) shown in the inset indicate the 16th to 84th percentile region of the fit posteriors, as shown by the violin plot (the orange shaded region). The density evolution that we assume for our fit, $n(M_{1450} < -26) \propto 10^{-k(z-6)}$, with $k = -0.7$, as well as the evolution assuming a value of $k = -0.78$, are shown as the solid and dashed dark gray lines, respectively. We compare our results to a large range of individual values from the literature, as indicated by the different markers and colors (Jiang et al. 2016; Yang et al. 2016; Akiyama et al. 2018; Matsuoka et al. 2018; McGreer et al. 2018; Giallongo et al. 2019; Schindler et al. 2019; Wang et al. 2019b; Boutsia et al. 2020; Onken et al. 2022; Pan et al. 2022), and to the density evolution from the QLFs of Richards et al. (2006; gray dotted line) and Kulkarni et al. (2019; gray dotted-dashed line). All data points, with the exception of the values from Jiang et al. (2016) and Wang et al. (2019b), are calculated by integrating the QLF model of the respective work. The other two values are determined in Wang et al. (2019b) using their Equation (12). We note the discrepancy between the majority of points and the number densities from Giallongo et al. (2019) and Boutsia et al. (2021), which are systematically higher. Given the most recent measurements at $z = 3-5$, our assumed value of $k = -0.7$ describes the increase of the luminous quasar density well from $z = 7$ to 3, without the need for a steeper ($k = -0.78$) evolution.

the Giallongo et al. (2019) QLF-based number densities shown in Figure 14 should be interpreted with caution.

Furthermore, we include the exponential density evolution with $k = -0.78$ (Wang et al. 2019a) and $k = -0.7$, anchored on our value as the dashed and solid gray lines in Figure 14. Pan et al. (2022) find a single value of $k = -0.7$ to describe the density evolution from $z = 3.5$ to $z = 5$. Based on our results, we argue that this evolution continues to $z \approx 7$, when excluding the discrepant data from Boutsia et al. (2021) and Giallongo et al. (2019). There is evidence that at $z < 4$ the density evolution flattens ($k > -0.7$), before the turnover point at $z \approx 2-2.5$ (Richards et al. 2006; Kulkarni et al. 2019), as also discussed in Onken et al. (2022). In light of the recent literature, and given the systematic uncertainties inherent in QLF estimates, due to differing models for completeness correction, we conclude that the bright-end density evolution at $z > 4$ can be well described by an exponential decline with $k = -0.7$. Comparing the work of Matsuoka et al. (2018) and our new estimate of the $z = 6$ quasar density with the value from Wang et al. (2019a), we do not find evidence for a more rapid decrease of the quasar density at $z > 6.5$, as originally reported from the comparison with the Jiang et al. (2016) quasar density in Wang et al. (2019a).

5.2. Forecasting High-redshift Quasar Detections

We explore the impact of our new QLF measurement on future high-redshift quasar detections. For this purpose, we use the Euclid mission (with an expected launch in 2023) as our main example. The Euclid wide-area survey will deliver Y -, J -, and H -band photometry down to a 5σ limiting magnitude of 24.0 mag (for point-like sources) over $\sim 15,000 \text{ deg}^2$. We use

`simqso` to simulate quasars and their photometry in the Euclid bands at $7 \leq z < 10$, according to our QLF over the wide-area survey footprint. The Ly α break at 1215 Å enters Euclid’s J band at $z \gtrsim 8.9$. Therefore, we require only $H < 24.0$ for a detection in the Euclid wide-area survey. We show the resulting detection number counts from our best-fit QLF model in comparison with the QLF models of Jiang et al. (2016), Matsuoka et al. (2018), and Wang et al. (2019b) in Table 6.

At $7 \leq z < 8$, we expect to probe an absolute magnitude of $M_{1450} \lesssim -22.4$. Therefore, the total number counts are strongly dependent on the faintest quasar population. While the Matsuoka et al. (2018) QLF and our measurement use the SHELLQs quasars to constrain the faint end, the Jiang et al. (2016) and Wang et al. (2019b) QLFs need to be extrapolated into this region. Hence, the predicted number counts based on their QLFs should be treated with this caveat in mind. Our work and the QLF from Matsuoka et al. (2018) produce similar predictions, whereas the steep faint-end slopes of the Jiang et al. (2016) and Wang et al. (2019b) QLFs lead to high quasar number counts in this redshift range. The overall slightly lower number densities of our QLF measurement compared to that of Matsuoka et al. (2018) make our predictions the least optimistic in this redshift range. At $8 \leq z < 9$ and $9 \leq z < 10$, the Euclid H -band magnitude probes $M_{1450} \lesssim -22.7$ and $M_{1450} \lesssim -23$, respectively. Due to the extrapolation to the faint end, the Jiang et al. (2016) QLF predicts the most optimistic number counts. At $8 \leq z < 9$, the expected quasar detections based on our measurement and the Matsuoka et al. (2018) and Wang et al. (2019b) QLFs are around 50–70. The numbers drop to 5–8 at the highest-redshift bin, where our new QLF measurement provides a more optimistic forecast. This simple forecast does not claim to present a comprehensive prediction of the quasar

Table 6
Forecasting Euclid Quasar Detections

QLF	k	$7 \leq z < 8$ $M_{1450} \lesssim -22.4$	$8 \leq z < 9$ $M_{1450} \lesssim -22.7$	$9 \leq z < 10$ $M_{1450} \lesssim -23.0$
This Work	-0.70	312	61	8
Matsuoka et al. (2018)	-0.70	360	49	5
Jiang et al. (2016)	-0.70	809	123	18
Wang et al. (2019b)	-0.78	668	71	5

Note. See Section 5.2 for details.

yields based on quasar selection strategies, as, for example, is presented by the Euclid Collaboration et al. (2019). In this context, our predicted detection numbers should be regarded as an upper limit to the number of quasars that could be discovered with Euclid, depending on the selection strategy. Our aim here is simply to illustrate how our new QLF measurement impacts our expectations for quasar discoveries. As the Euclid Collaboration et al. (2019) selection predictions are based on the Jiang et al. (2016) QLF, their resulting quasar yields are likely too optimistic in light of our new QLF measurement.

5.3. Quasar Contribution to Hydrogen Reionization

Based on our new measurement of the QLF at $z \sim 6$, we calculate the quasar contribution to the H I photoionization rate of the UV background. Following the literature (e.g., Haardt & Madau 1996, 2012; Faucher-Giguère 2020), the H I photoionization rate is

$$\Gamma_{\text{HI}}(z) = \int_{\nu_{912}}^{\infty} d\nu \sigma_{\text{HI}}(\nu) c n_{\nu}(\nu, z), \quad (27)$$

where $\sigma_{\text{HI}}(\nu)$ is the frequency-dependent H I photoionization cross section and $n_{\nu}(\nu, z)$ is the number density of the ionizing photons per unit frequency at redshift z . The lower boundary of the integral ν_{912} corresponds to the frequency at a wavelength of 912 Å. At $z=6$, we can assume that the optical depth of the ionizing photons is smaller than unity, $\tau_{\text{eff}} \leq 1$, allowing us to adopt the “local source” approximation (e.g., Zuo & Phinney 1993; Madau et al. 1999), simplifying $n_{\nu}(\nu, z)$ to

$$n_{\nu}(\nu, z) \approx \frac{(1+z)^3}{h\nu} \frac{l(\nu, z)}{c} \epsilon(\nu, z). \quad (28)$$

In the equation above, $l(\nu, z)$ is the mean free path of the ionizing photons and $\epsilon(\nu, z)$ is the comoving emissivity of the ionizing sources. We closely follow Shen et al. (2020) in adopting the frequency dependence on the mean free path, based on the results of Faucher-Giguère et al. (2008), $l(\nu, z) = l(\nu_{912}, z)(\nu/\nu_{912})^{3(\beta-1)}$, where the power-law index of the intergalactic H I column density distribution is assumed to be $\beta=1.5$ (Madau et al. 1999). Furthermore, we also assume a power-law shape for the extreme UV quasar continuum, with an index of $\alpha_{\text{UV}}=1.7$ (Lusso et al. 2015):

$$\epsilon(\nu, z) = \epsilon_{912}(z) \left(\frac{\nu}{\nu_{912}} \right)^{-\alpha_{\text{UV}}}. \quad (29)$$

Assuming a frequency dependence of $\sigma_{\text{HI}} \propto \nu^{-3}$, we analytically integrate Equation (27), which yields

$$\Gamma_{\text{HI}}(z) \approx \frac{(1+z)^3}{3 + \alpha_{\text{UV}} - 3(\beta-1)} \epsilon_{912}(z) l(\nu_{912}, z) \sigma_{\text{HI}}(\nu_{912}). \quad (30)$$

For the H I photoionization cross section, we use a value of $\sigma_{\text{HI}}(\nu_{912}) = 6.35 \times 10^{-18} \text{ cm}^2$ (Verner et al. 1996; Becker et al. 2015a).

Using our new measurement of the QLF, we first calculate the ionizing emissivity of the quasars at 1450 Å:

$$\epsilon_{1450}(z) = \int_{-\infty}^{-18} \Phi(M_{1450}, z) L_{1450}(M_{1450}) dM_{1450}. \quad (31)$$

Here, we assume that the escape fraction of ionizing photons from the type-1 quasar population measured by the QLF is unity. We adopt an upper integration boundary (faint limit) of $M_{1450} = -18$ for comparison with the recent literature (Matsuoka et al. 2018; Kulkarni et al. 2019; Wang et al. 2019b). Assuming a power-law spectral energy distribution for the quasars in the extreme UV (Lusso et al. 2015),

$$f_{\nu} \propto \begin{cases} \nu^{-0.61} & \forall \lambda > 912 \text{ Å} \\ \nu^{-1.70} & \forall \lambda < 912 \text{ Å} \end{cases}, \quad (32)$$

we estimate the ionizing emissivity at 912 Å as

$$\epsilon_{912}(z) = \epsilon_{1450}(z) \times (1450 \text{ Å}/912 \text{ Å})^{-0.6}. \quad (33)$$

Based on our fiducial DPL fit to the combined PS1+ SHELLQs quasar sample, we calculate a value of $\epsilon_{912}(z=6) = 7.23^{+1.65}_{-1.02} \times 10^{22} \text{ erg s}^{-1} \text{ Hz}^{-1} \text{ cMpc}^{-3}$. The errors reflect the statistical fit uncertainty on the QLF as corresponding to the 16%–84% percentile range. Figure 15 shows our result in comparison with values from the recent literature. Our quasar sample is dominated by the SHELLQs quasar sample at the faint end, which strongly affects the ionizing emissivity. In comparison with other studies of the type-1 UV QLF at $z=6$, this fact largely explains the disagreement with the values of Jiang et al. (2016), Parsa et al. (2018), and Kulkarni et al. (2019), as well as the agreement with the work of Matsuoka et al. (2018). Furthermore, our best-fit QLF model has a steeper bright-end slope than all previous measurements, reducing the integrated emissivity of the luminous quasar contribution as well.

In order to calculate the photoionization rate based on our QLF measurement, we need to adopt a value for the mean free path of ionizing photons at $z \approx 6$. Becker et al. (2021) recently measured the mean free path of ionizing photons and found a value of $l(\nu_{912}, z=6) = 0.75^{+0.65}_{-0.45} \text{ pMpc}$ at $z=6$, which falls

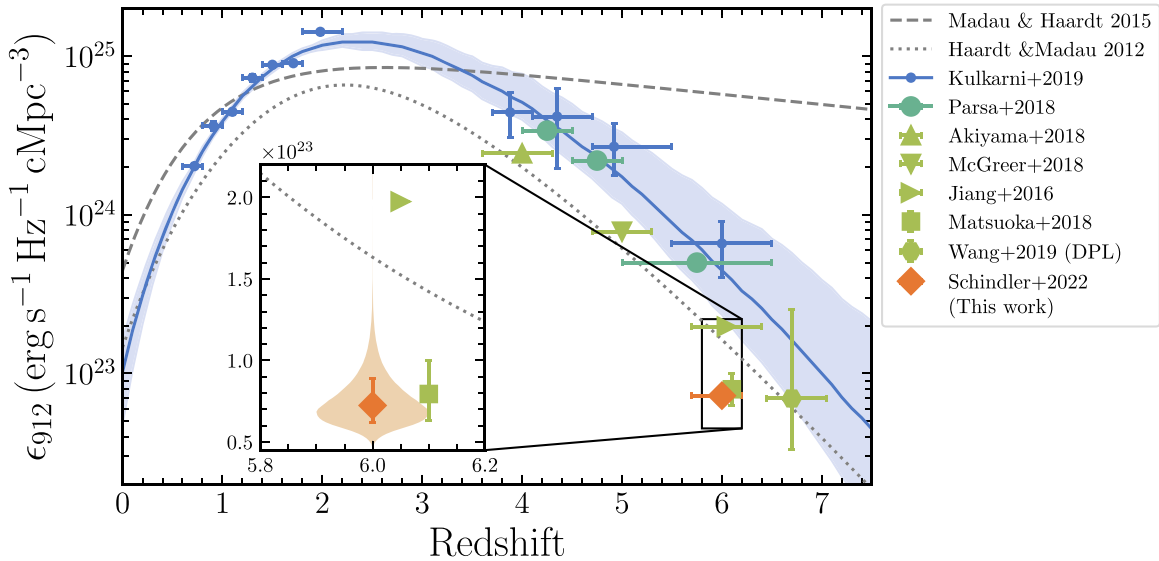


Figure 15. The quasar ionizing emissivity at 912 Å as a function of redshift. The ionizing emissivity is derived from Equation (31), with a faint luminosity limit of $M_{1450} = -18$. We show our result as the orange diamond. The error bars in the inset indicate the 16th to 84th percentile region of the fit posteriors, which are shown by the violin plot (the orange shaded region). We compare our data to various results in the literature (Jiang et al. 2016; Akiyama et al. 2018; Matsuoka et al. 2018; McGreer et al. 2018; Parsa et al. 2018; Kulkarni et al. 2019; Wang et al. 2019a). We include the individual data points from Kulkarni et al. (2019) that were not affected by systematic errors, as discussed by the authors. The horizontal error bars on the individual data points indicate the redshift ranges of the different QLF samples. The solid blue line and the blue shaded area show the derived posterior median emissivity evolution model and the 1σ uncertainties of Kulkarni et al. (2019). We also display the models by Haardt & Madau (2012) and Madau & Haardt (2015). Our derived quasar emissivity falls well below other measurements at $z = 6$, with the exception of the work of Matsuoka et al. (2018), with which we share the SHELLQs quasar sample at the faint end.

below extrapolations from lower redshift. We adopt this value, noting that these measurements are in agreement with the independently calculated lower limits reported by Bosman (2021).

With these assumptions, we calculate a quasar photoionization rate of $\Gamma_{\text{H I}}(z = 6) = 5.86^{+5.08+1.33}_{-3.51-0.83} \times 10^{-16} \text{ s}^{-1}$. The first errors reflect the 1σ uncertainties of the mean free path (Becker et al. 2021), while the second errors are due to the statistical 1σ uncertainty in the QLF DPL fit. The total photoionization rate at $z \approx 6$ has been measured to be $\Gamma_{\text{H I}}(z = 6) \approx 10^{-13} \text{ s}^{-1}$, based on quasar near-zone sizes (Calverley et al. 2011; Wyithe & Bolton 2011) and the mean transmitted Ly α flux from quasar spectra (D’Aloisio et al. 2018; Davies et al. 2018). As a combination of our low-emissivity values, based on our new QLF measurement, and the short mean free path of Becker et al. (2021), the quasar contribution to the photoionization rate is roughly 2 orders of magnitude lower than the total value. This result strongly disfavors the dominant contribution of quasars to cosmic hydrogen reionization at high redshifts, in line with other recent studies of the high-redshift QLF (Jiang et al. 2016, 2022; Matsuoka et al. 2018; McGreer et al. 2018; Parsa et al. 2018; Kulkarni et al. 2019; Wang et al. 2019a).

5.4. Quasar Lensing and the QLF

None of the 125 quasars in our sample are known to be gravitationally lensed by a foreground galaxy. This is a direct consequence of our selection criteria (Section 2.2). Our morphology selection criterion aims at selection point sources, and thus naturally excludes lensed quasars, which appear extended if they consist of multiple source images or if a foreground lens galaxy is detected. In addition, the required color criteria are designed to select quasars using the Ly α break. In the event that a foreground lens galaxy contaminates

the bluer bands, the criteria bias against the selection of such sources.

Following the serendipitous discovery of the highest-redshift lensed quasar, J043947.08+163415.7, at $z = 6.51$ (Fan et al. 2019), Pacucci & Loeb (2019) reevaluated the theoretical consequences of this discovery and concluded that a large fraction of quasars at $z > 6$ were being missed by current surveys. For a bright-end slope of $\beta = -3.6$, the authors expected about half of the $z > 6$ population to be lensed. The steep bright-end slope of $\beta = -3.84$ resulting from our new QLF measurement would lead to an even larger lensed fraction of the $z > 6$ quasar population. In consequence, our bright-end slope measurement would strongly suggest that we are missing a large fraction of lensed quasars. Given that only one lensed quasar at $z > 6$ has been discovered (Fan et al. 2019), our bright-end slope measurement and the resulting lensed fraction, according to Pacucci & Loeb (2019), is in strong tension with the observations.

The recent study by Yue et al. (2022) revisits the predicted fraction of high-redshift lensed quasars. By adopting recent galaxy velocity dispersion functions that affect the lensing optical depth, they conclude that the lensed fraction for bright quasars at $z \sim 6$ can reach 2%–6%, depending on the QLF bright-end slope. Following their Figure 5, and adopting $M_{\text{lim}} - M^* \approx 1 \text{ mag}$ for the PS1 quasar selection, results in a lensed fraction of $\lesssim 1\%$ for $\beta \approx -4$. In line with the observations (Fan et al. 2019), this result suggests that even with our steep bright-end slope, we would have found only ~ 1 lensed quasar with our selection, had not it been biased against these sources.

6. Conclusions

In this work, we present the most precise measurement of the $z \approx 6$ QLF at $-28 \lesssim M_{1450} \lesssim -22$ to date, based on a combined

sample of 121 quasars from the PS1 $z > 5.6$ quasar survey and 48 quasars from SHELLQs. We determine the full PS1 quasar survey completeness, taking into account the different components of the PS1 quasar selection strategy and the state of the spectroscopic observations. We use an ML approach (see Appendix A), sampled via MCMC, in order to fit a DPL QLF model to the quasar data. Our fiducial model (Table 4, first row) is determined using the combined quasar sample and assumes the exponential evolution of the quasar density, with $k = -0.7$. The four best-fit parameters are $\log(\Phi^*(z=6)/\text{Mpc}^{-3} \text{mag}^{-1}) = -8.75^{+0.47}_{-0.41}$, $M^* = -26.38^{+0.79}_{-0.60} \text{mag}$, $\alpha = -1.70^{+0.29}_{-0.19}$, and $\beta = -3.84^{+0.63}_{-1.21}$. The combined PS1 and SHELLQs quasar sample constrains the break magnitude to be $\sim 1 \text{mag}$ brighter and the bright-end slope to be significantly steeper than previous studies at this redshift (Willott et al. 2010; Jiang et al. 2016; Matsuoka et al. 2018).

Using our fiducial QLF model, we calculate the bright-end quasar density, $n(M_{1450} < -26, z = 5.85) = 1.16^{+0.13}_{-0.12} \text{cGpc}^{-3}$, and put it in perspective with its redshift evolution at $z \approx 4-7$. We find that an exponential density evolution model, with an exponent of $k = -0.7$, as assumed in our QLF fit, describes the literature data over this redshift range well, without the need for an accelerating decline of the quasar density at $z > 6.5$, as proposed by Wang et al. (2019b).

With our fiducial QLF model, we derive the ionizing emissivity of the quasar population and their contribution to cosmic hydrogen reionization. Using standard assumptions, we calculate the ionizing emissivity to be $\epsilon_{912}(z=6) = 7.23^{+1.65}_{-1.02} \times 10^{22} \text{erg s}^{-1} \text{Hz}^{-1} \text{cMpc}^{-3}$. This result is lower than some previous results (e.g., Jiang et al. 2016), but it shows good agreement with Matsuoka et al. (2018), the most recent estimate of the $z \approx 6$ QLF. Adopting the mean free path of Becker et al. (2021), the only measurement at $z \approx 6$, we estimate an HI quasar photoionization rate 2 orders of magnitude below estimates of its total value, strongly disfavoring quasars as being the dominant driver of hydrogen reionization at $z \approx 6$.

The authors would like to thank the anonymous referee for the insightful comments that helped to improve the manuscript. We would further like to thank Sarah E. I. Bosman, Joseph F. Hennawi, and Romain Meyer for fruitful discussions and comments on the manuscript. J.T.S. and R.N. acknowledge funding from the European Research Council (ERC) Advanced Grant program under the European Union’s Horizon 2020 research and innovation program (grant agreement No. 885301). The work of T.C. and D.S. was carried out at the Jet Propulsion Laboratory, California Institute of Technology, under a contract with the National Aeronautics and Space Administration (80NM0018D0004). T.C.’s research was supported by an appointment to the NASA Postdoctoral Program at the Jet Propulsion Laboratory, California Institute of Technology, administered by the Universities Space Research Association, under contract with NASA. E.P.F. is supported by the international Gemini Observatory, a program of NSF’s NOIRLab, which is managed by the Association of Universities for Research in Astronomy (AURA), under a cooperative agreement with the National Science Foundation, on behalf of the Gemini partnership of Argentina, Brazil, Canada, Chile, the Republic of Korea, and the United States of America. Some of the results in this paper have been derived using the healpy and HEALPix package. The Pan-STARRS1 (PS1) Survey and the PS1 public science archive

have been made possible through contributions from the Institute for Astronomy, the University of Hawaii, the Pan-STARRS Project Office, the Max-Planck Society and its participating institutes, the Max Planck Institute for Astronomy, Heidelberg, and the Max Planck Institute for Extraterrestrial Physics, Garching, the Johns Hopkins University, Durham University, the University of Edinburgh, the Queen’s University Belfast, the Harvard-Smithsonian Center for Astrophysics, the Las Cumbres Observatory Global Telescope Network Incorporated, the National Central University of Taiwan, the Space Telescope Science Institute, the National Aeronautics and Space Administration, under grant No. NNX08AR22G, issued through the Planetary Science Division of the NASA Science Mission Directorate, the National Science Foundation, under grant No. AST-1238877, the University of Maryland, Eotvos Lorand University (ELTE), the Los Alamos National Laboratory, and the Gordon and Betty Moore Foundation.

Software: Astropy (Astropy Collaboration et al. 2013, 2018), chainconsumer (Hinton 2016), Numpy (van der Walt et al. 2011; Harris et al. 2020), healpy (Zonca et al. 2019), Pandas (McKinney 2010; Pandas Development Team 2020), SciPy (Virtanen et al. 2020), emcee (Foreman-Mackey et al. 2013).

Appendix A Mathematical Formulation of the QLF Analysis

The QLF $\Phi(M_{1450}, z)$ describes the number density of quasars as a function of their absolute magnitude at 1450 Å, M_{1450} , and redshift z . To derive the QLF, it is imperative to take into account the selection effects that are inherent in the parent catalog data and that are imposed by the selection criteria for the quasar discovery survey (see Section 2.2). The selection function $S(\mathbf{q})$ describes the probability of a source with attributes \mathbf{q} being within the given sample. In this section, we explicitly derive the mathematical formulation of our MCMC ML analysis of the QLF.

A.1. The Quasar Incidence as Predicted by the QLF

We begin our discussion by closely following Rix et al. (2021, their Equation (1)) in describing the expected catalog incidence $d\Lambda(\mathbf{q})$ of quasars in our sample, through the selection function $S(\mathbf{q})$ multiplied with a model family for quasars $\mathcal{M}(\mathbf{q}|\Theta_{\text{mod}})$, parameterized by Θ_{mod} :

$$d\Lambda(\mathbf{q}) = \mathcal{M}(\mathbf{q}|\Theta_{\text{mod}}) S(\mathbf{q}) d\mathbf{q}. \quad (\text{A1})$$

In our case, the QLF Φ forms the basis of the model family. In its most general form, the QLF can be written as a function of the luminosity (in our case, the absolute magnitude at 1450 Å), the 3D position of the quasars $\mathbf{x} = (r, \theta, \phi)$ (in spherical coordinates), and the QLF parameters Θ_{QLF} . The distance to the quasars r is not a direct observable. Therefore, it is much more practical (and common) to formulate the QLF as a function of the redshift z . Furthermore, we have good reason to assume that our universe is isotropic on large scales. In this case, the QLF is independent of sky position (θ, ϕ) . However, the selection function may depend on the sky position, and thus we separate the sky dependence from the QLF using the unit normal vector $\hat{n}(\theta, \phi)$:

$$\begin{aligned} \mathcal{M}(\mathbf{q}|\Theta_{\text{mod}}) \\ = \Phi(M_{1450}, z, \theta, \phi|\Theta_{\text{QLF}}) = \Phi(M_{1450}, z|\Theta_{\text{QLF}}) \hat{n}(\theta, \phi). \end{aligned} \quad (\text{A2})$$

For the clarity of the mathematical expressions, we omit the subscript for the absolute magnitude at 1450 Å, M_{1450} , in the following, and simply denote it with M . We now substitute Equation (A2) into Equation (A1), and integrate both sides over the volume (dV) and absolute magnitude (dM), to retain the total expected number of quasars as observed, given the model and the selection function:

$$\Lambda(M, z, \theta, \phi) = \int_M^{M+\Delta M} \int_V \Phi(M, z|\Theta_{\text{QLF}}) \times \hat{n}(\theta, \phi) S(\mathbf{q}(M, z, \theta, \phi)) dV(z|\Theta_{\text{Cos}}) dM. \quad (\text{A3})$$

Due to the redshift dependency of the QLF, executing the volume integral requires a cosmological model with its own range of parameters Θ_{Cos} . We will now rewrite the volume integral in terms of the differential comoving solid volume element ($dV/dz/d\Omega$), a standard quantity in any cosmological model:

$$dV(z|\Theta_{\text{Cos}}) = \frac{dV}{dzd\Omega}(z|\Theta_{\text{Cos}}) dzd\Omega. \quad (\text{A4})$$

Substituting Equation (A4) into Equation (A3) allows us to separate the volume integration into integrals over redshift and solid angle:

$$\Lambda(M, z, \theta, \phi) = \int_{\Omega} \int_M^{M+\Delta M} \int_z^{z+\Delta z} \Phi(M, z|\Theta_{\text{QLF}}) \frac{dV}{dzd\Omega}(z|\Theta_{\text{Cos}}) \hat{n}(\theta, \phi) \times S(\mathbf{q}(M, z, \theta, \phi)) dzdM d\Omega. \quad (\text{A5})$$

For surveys of inhomogeneous depth, it can often be difficult to find an analytic expression for the sky position dependence of the selection function. In this work, we take the inhomogeneity into account when modeling the observed quasar properties by sampling from the depth distribution. Therefore, we continue as one would with a survey of homogeneous depth and drop the sky position dependence. Now, the integral over the survey footprint simply yields the total footprint area Ω :

$$\Lambda(M, \Delta M, z, \Delta z) = \Omega \int_M^{M+\Delta M} \int_z^{z+\Delta z} \Phi(M, z|\Theta_{\text{QLF}}) \frac{dV}{dzd\Omega}(z|\Theta_{\text{Cos}}) S(\mathbf{q}(M, z)) dzdM. \quad (\text{A6})$$

Given a model for the QLF $\Phi(M, z|\Theta_{\text{QLF}})$, a cosmological model Θ_{Cos} , and a model of the observed properties given the absolute magnitude and redshift $\mathbf{q}(M, z)$, we can now calculate the total expected number of observed quasars as a function of the absolute magnitude and redshift.

A.2. Formulating the Likelihood Function

We derive the likelihood function for the QLF analysis following Marshall et al. (1983) and Fan et al. (2001b). The probability of detecting n_{lm} quasars, given the QLF $\Phi(M, z|\Theta_{\text{QLF}})$, in an absolute magnitude bin $(\Delta M)_l$ and redshift bin $(\Delta z)_m$ can be written in terms of the Poisson distribution

function, using the incidence rate $\Lambda_{lm}(M, z)$ of Equation (A6):

$$P(n_{lm}|\Phi(M, z|\Theta_{\text{QLF}})) = \frac{\Lambda_{lm}(M, z)^{n_{lm}} e^{-\Lambda_{lm}(M, z)}}{n_{lm}!}. \quad (\text{A7})$$

The probability of finding $N(M, z)$ quasars in the entire survey, as characterized by the full absolute magnitude and redshift range, can then be written as the product of the probabilities over all absolute magnitude and redshift bins:

$$\begin{aligned} P(N(M, z)|\Phi(M, z|\Theta_{\text{QLF}})) &= \prod_{lm} \frac{\Lambda_{lm}(M, z)^{n_{lm}} e^{-\Lambda_{lm}(M, z)}}{n_{lm}!} \\ &= \prod_{lm}^{n_{lm}=1} \Lambda_{lm}(M, z) e^{-\Lambda_{lm}(M, z)} \\ &\times \prod_{lm}^{n_{lm}=0} e^{-\Lambda_{lm}(M, z)} \\ &= \prod_{lm}^{n_{lm}=1} \Lambda_{lm}(M, z) \times \prod_{lm} e^{-\Lambda_{lm}(M, z)}. \end{aligned} \quad (\text{A8})$$

If the absolute magnitude and redshift bins are infinitesimally small, then either $n_{lm} = 1$ or $n_{lm} = 0$ quasars can be found in each bin. We split the product into two terms for these two cases, simplifying the equation. We can furthermore rearrange the terms, to arrive at the final version of the probability $P(N(M, z)|\Phi(M, z|\Theta_{\text{QLF}}))$ in Equation (A8). Our main goal is to constrain the QLF $\Phi(M, z|\Theta_{\text{QLF}})$ and its parameters Θ_{QLF} , based on the observed distribution of high-redshift quasars $N(M, z)$. We are basically asking what the probability of $\Phi(M, z|\Theta_{\text{QLF}})$ is, given $N(M, z)$ observed quasars in the interval $\Delta M \Delta z$ and in the survey area Ω :

$$\begin{aligned} P(\Phi(M, z|\Theta_{\text{QLF}})|N(M, z)) \\ = P(N(M, z)|\Phi(M, z|\Theta_{\text{QLF}})) \frac{P(\Phi(M, z|\Theta_{\text{QLF}}))}{P(N(M, z))}. \end{aligned} \quad (\text{A9})$$

Assuming flat priors for $N(M, z)$ and $\Phi(M, z|\Theta_{\text{QLF}})$, we can simplify the probability of $\Phi(M, z|\Theta_{\text{QLF}})$, given $N(M, z)$, to

$$\begin{aligned} P(\Phi(M, z|\Theta_{\text{QLF}})|N(M, z)) \\ \propto P(N(M, z)|\Phi(M, z|\Theta_{\text{QLF}})). \end{aligned} \quad (\text{A10})$$

We have already discussed how to express the second term in this equation via the incidence rate in Equation (A8). We now formulate the logarithmic probability equivalent to the logarithmic likelihood:

$$\begin{aligned} \ln[P(\Phi(M, z|\Theta_{\text{QLF}})|N(M, z))] \\ \propto \ln[P(N(M, z)|\Phi(M, z|\Theta_{\text{QLF}}))] \\ \propto \sum_{lm}^{n_{lm}=1} \ln[\Lambda_{lm}(M, z)] - \sum_{lm} \Lambda_{lm}(M, z). \end{aligned} \quad (\text{A11})$$

To evaluate this equation further, we will take a look at the incidence rate $\Lambda_{lm,j}(M, z)$ for a single quasar j . The quasar j has an absolute magnitude M_j and redshift z_j in bin centers of width $(\Delta M)_l$ and $(\Delta z)_m$. With these boundary conditions, we can

write Equation (A6) for a single quasar as

$$\Lambda_{lm,j}(M, z) = \int_{M_j - (\Delta M)_l/2}^{M_j + (\Delta M)_l/2} \int_{z_j - (\Delta z)_m/2}^{z_j + (\Delta z)_m/2} \Phi(M, z | \Theta_{\text{QLF}}) \frac{dV}{dz d\Omega} (z | \Theta_{\text{Cos}}) S(\mathbf{q}(M, z)) dz dM \Omega. \quad (\text{A12})$$

In the limit of infinitesimal bin sizes around M_j and z_j , the integrals can be trivially evaluated and we can drop the indices l and m :

$$\Lambda_j(M, z) = \Phi(M_j, z_j | \Theta_{\text{QLF}}) \frac{dV}{dz d\Omega} \times (z_j | \Theta_{\text{Cos}}) S_j(\mathbf{q}(M_j, z_j)) (\Delta z)_m (\Delta M)_l \Omega. \quad (\text{A13})$$

Starting from the first term of the right-hand side of Equation (A11), we first rewrite the sum over all bins l and m for which $n_{lm} = 1$ as the sum over all $N(M, z)$ quasars in the data set. We then apply the natural logarithm to Equation (A13) and, equivalent to Marshall et al. (1983), we drop all terms independent of the QLF and the selection function, which would only add constant values to the logarithmic probability:

$$\sum_{lm} \ln [\Lambda_{lm}(M, z)] = \sum_{j=1}^{N(M,z)} \ln [\Lambda_j(M, z)] \times \propto \sum_{j=1}^{N(M,z)} \ln [\Phi(M_j, z_j | \Theta_{\text{QLF}}) S_j(\mathbf{q}(M_j, z_j))]. \quad (\text{A14})$$

The second term in Equation (A11) normalizes the logarithmic probability, by summing over the full interval in the absolute

magnitude ΔM and redshift Δz for which we aim to evaluate the QLF. By choosing the appropriate integration boundaries for the QLF evaluation in Equation (A6), we can simplify the expression to

$$\sum_{lm} \Lambda_{lm}(M, z) = \Lambda(M, z). \quad (\text{A15})$$

The logarithmic probability of $\Phi(M, z | \Theta_{\text{QLF}})$, given $N(M, z)$, our likelihood function, can then be approximated by

$$\ln [P(\Phi(M, z | \Theta_{\text{QLF}}) | N(M, z))] \propto \sum_{j=1}^{N(M,z)} \ln [\Phi(M_j, z_j | \Theta_{\text{QLF}}) S_j(\mathbf{q}(M_j, z_j))] - \Lambda(M, z), \quad (\text{A16})$$

with $\Lambda(M, z)$ as in Equation (A6).

Appendix B Extended Discussion of the Quasar Model

To test the robustness of our `simqso` quasar model, we compare its synthetic photometry to the recently published `qsogen` model by Temple et al. (2021). The latter has been used in the prediction of quasar yields for the Euclid mission (Euclid Collaboration et al. 2019). At the core of `qsogen` is a parametric quasar spectral model, which has been fit to optical to near-IR colors of a subsample of SDSS DR16 quasars (Lyke et al. 2020). Equivalent to the `simqso` quasar model, the `qsogen` quasar model is explicitly designed to reproduce the median quasar colors of real sources. A particular novel feature of `qsogen` is the emission line quasar templates, which allow the diversity of quasar line strengths and velocity shifts to be

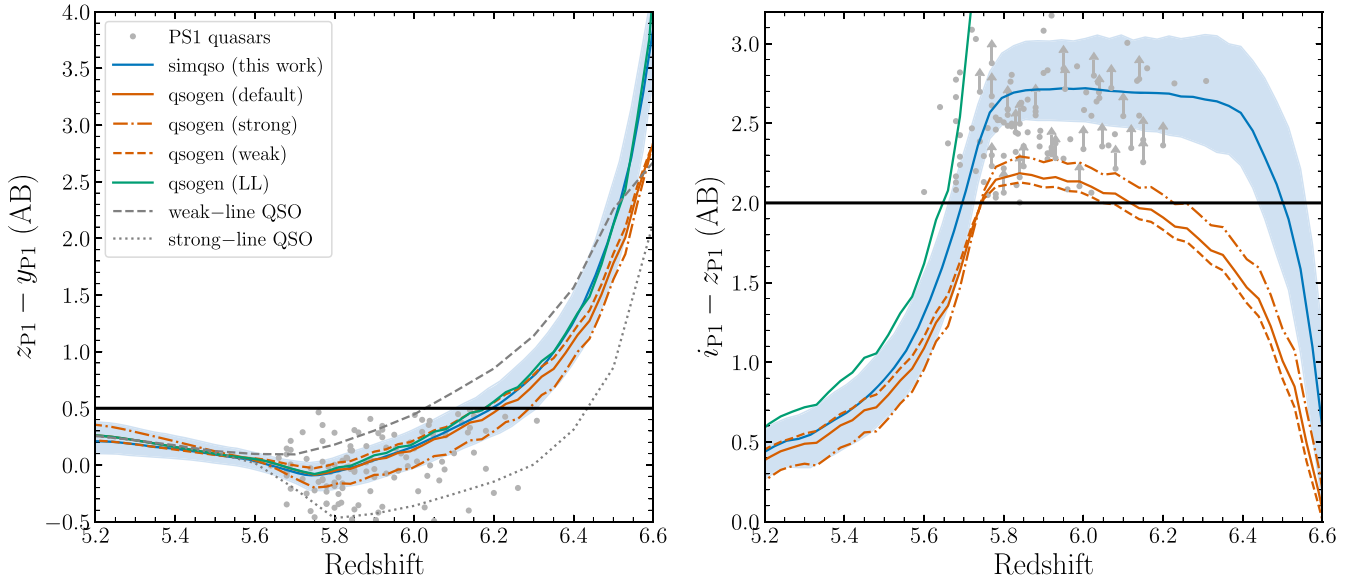


Figure 16. Left: synthetic quasar $z_{\text{P1}} - y_{\text{P1}}$ color as a function of redshift. The median quasar color from the `simqso` sample that is used to derive the selection function is shown in blue, with the blue shading indicating the 5th–95th percentile range. The quasar colors modeled with `qsogen` (Temple et al. 2021) are shown in orange for the default model (the solid line), for a model with weak line emission (the dashed line), and for a model with strong line emission (the dashed–dotted line). The green line depicts an alternative to the `qsogen` default model, where an LL system at the redshift of the quasar absorbs all flux blueward of 1215 Å, mimicking full Gunn–Peterson absorption blueward of the Ly α line. The PS1 dereddened colors of the PS1 quasar sample are shown as the gray points. The solid black line shows the dividing line for the $z_{\text{P1}} - y_{\text{P1}} < 0.5$ color criterion. In addition, we show the color redshift evolutions of the WLQ and strong-line quasar templates from Bañados et al. (2016; the blue and red spectra in their Figure 10). At $z \gtrsim 6.3$, the color is biased blue by the nonevolving IGM transmission in the templates. Right: synthetic quasar $i_{\text{P1}} - z_{\text{P1}}$ color as a function of redshift. The symbols are the same, with the addition of the solid black line that depicts the $i_{\text{P1}} - z_{\text{P1}} > 2$ color criterion used in this work.

captured, and which can be modified via the `emline_type` argument, which has a default value of -0.9936 .

The quasar selection criteria on which our new QLF measurement is based rely on color cuts in the reddest PS1 filter bands— i_{P1} , z_{P1} , and y_{P1} . We use `qsogen` to calculate the magnitudes in these bands, then compare the resulting $i_{P1} - z_{P1}$ and $z_{P1} - y_{P1}$ colors between `qsogen` and our quasar model, based on `simqso`. To capture the quasar diversity in terms of emission line properties with `qsogen`, we produce three models: (1) the *default* model uses the default value of `emline_type`; (2) the *strong* emission line model uses `emline_type=1`; and (3) the *weak* emission line model uses `emline_type=-1`. We compare the resulting colors as a function of redshift in Figure 16. The $z_{P1} - y_{P1}$ color of our quasar model and the `qsogen` models is consistent over $z = 5.2$ – 5.8 . The diversity of quasar colors due to the different `qsogen` emission line models is well captured by the random sampling of continuum and emission line properties in `simqso` (Section 3.1.1). Small differences in the $z_{P1} - y_{P1}$ color appear at $z > 5.8$, which increase toward $z = 6.6$. We attribute these differences to the different prescriptions for the absorption of neutral hydrogen due to the IGM, which become more pronounced at $z > 5.8$ as the Ly α line moves to the red side of the z_{P1} filter band. The selection of $z > 5.7$ quasars is based on a color dropout selection, requiring $i_{P1} - z_{P1} > 2$. The right panel of Figure 16 shows $i_{P1} - z_{P1}$ as a function of redshift, and highlights the dropout criterion with the solid black line. Quasars with colors above the black line would be selected. With our `simqso` quasar model, we start to select quasars at $z > 5.6$ (the solid blue line and the blue shaded region). The downturn of the $i_{P1} - z_{P1}$ color at $z \gtrsim 6.4$ is due to the Ly α line moving out of the z_{P1} filter band. As a consequence, little to no quasar flux is measured in both the i_{P1} and z_{P1} bands. Our `simqso` quasar model mostly agrees with the `qsogen` models at $z \lesssim 5.6$. However, once the Ly α line leaves the i_{P1} band ($z \gtrsim 5.6$), color differences become evident. We argue that these are mainly caused by the different prescriptions for IGM absorption in the spectral models. While

`simqso` uses the stochastic Ly α forest model of McGreer et al. (2013; see Section 3.1.1), `qsogen` uses a prescription based on Becker & Bolton (2013). Compared to our `simqso` model, the `qsogen` spectra have more flux blueward of Ly α , resulting in a generally bluer color. When compared the to quasars selected in this work (the gray points), the `simqso` IGM model provides a better representation of the empirical data points.¹⁴ The `qsogen` models show significantly bluer $i_{P1} - z_{P1}$, especially at $z > 5.6$. Introducing a Lyman limit (LL) system at the redshift of the quasar (i.e., at a rest-frame wavelength of 1215 Å) to the `qsogen` default model effectively reduces all blueward flux to zero. At $z \lesssim 6.0$, this approach is unphysical, as the flux blueward of Ly α can be transmitted in ionized patches of the IGM. However, it is a valid assumption at higher redshifts (see, e.g., at $z > 7$; Euclid Collaboration et al. 2019). We show this `qsogen` LL model as the green line in Figure 16. The `qsogen` LL model has a significantly redder $i_{P1} - z_{P1}$ color at $z < 5.7$, which diverges further at $z \approx 5.7$. Compared to the PS1 quasar photometry at $z \approx 5.6$ – 6.4 , it is not a good representation of the data. However, the resulting $z_{P1} - y_{P1}$ color of our quasar model and of `qsogen` are now fully consistent over the entire redshift range. This agreement in the $z_{P1} - y_{P1}$ color shows that, barring the differences in prescription for IGM absorption, both our `simqso` quasar model and the `qsogen` model produce consistent median colors, as expected from their design goals.

Appendix C Supplemental Figures

Here, we present a number of figures that provide supplemental information for a few sections of the paper. Figure 17 shows the spectroscopic identification completeness for quasar samples with visual ranks 2, 3, and 4, separately. For context—that is, the covariance of the different QLF parameters in our ML fit—we provide the full covariance matrix in Figure 18. Analogous to Figure 3, we also show the PS1 y-band limiting magnitude as a function of survey area in Figure 19.

¹⁴ One might be concerned that the `simqso` synthetic colors do not encompass the full $i_{P1} - z_{P1}$ color scatter of the PS1 quasars. We note that the synthetic color range is broadened significantly by the PS1 photometric uncertainties (Section 3.1.2), before the selection function is assessed.

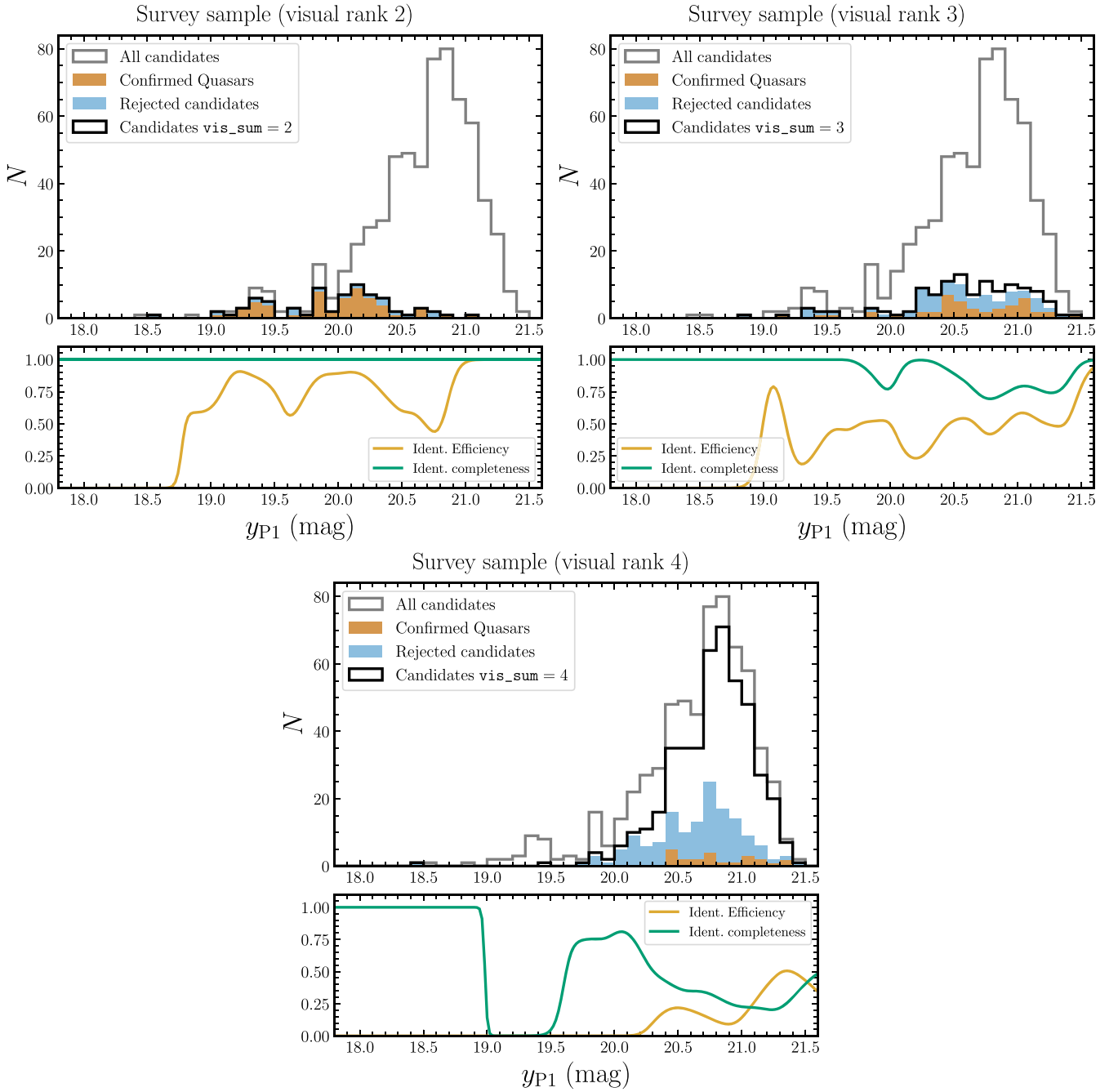


Figure 17. In these three panels, we show the observed survey samples, their selection efficiency, and their identification completeness, for the three different visual ranks. Comparing the samples reveals that the majority of the remaining candidates have the worst visual rank ($\text{vis_sum} = 4$) and the lowest selection efficiency. Our identification completeness (Equation (15)) takes these differences into account.

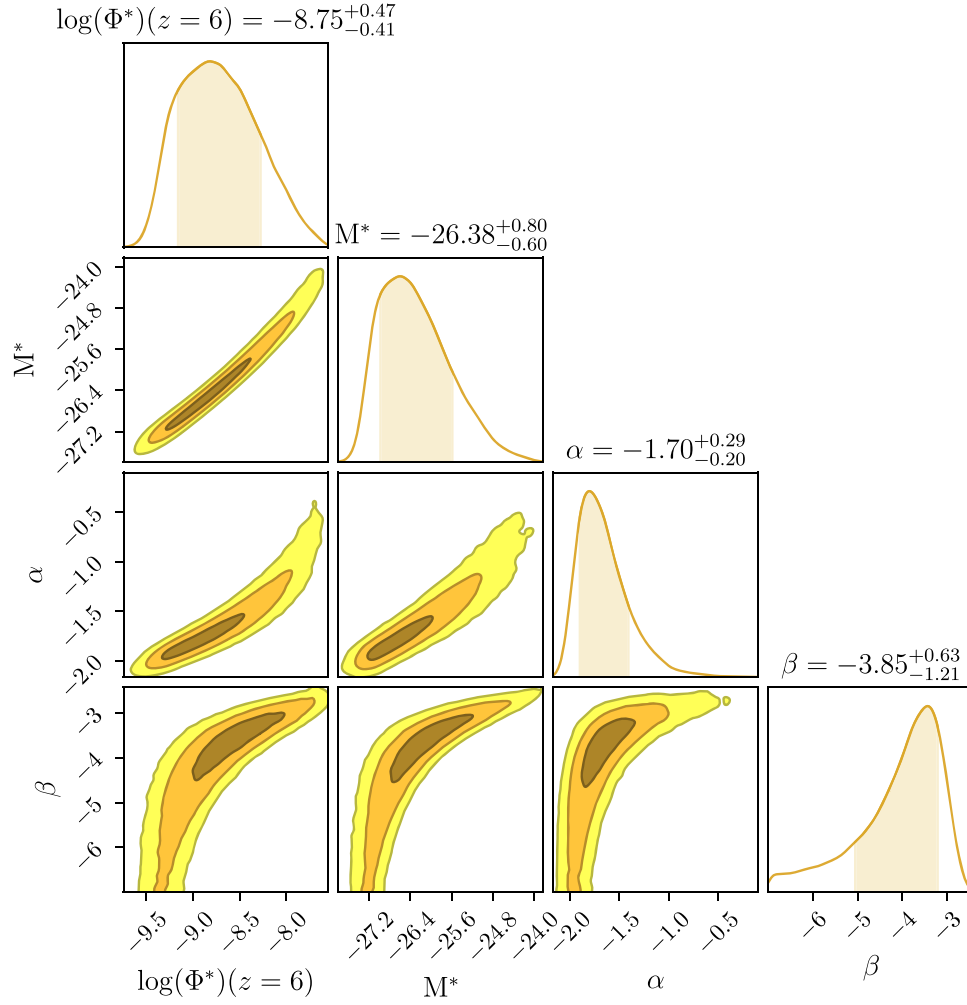


Figure 18. Covariance matrix of the fiducial DPL QLF fit to the combined PS1 + SHELLQs quasar sample (Table 4, first row). The contours highlight the 1σ , 2σ , and 3σ confidence bounds.

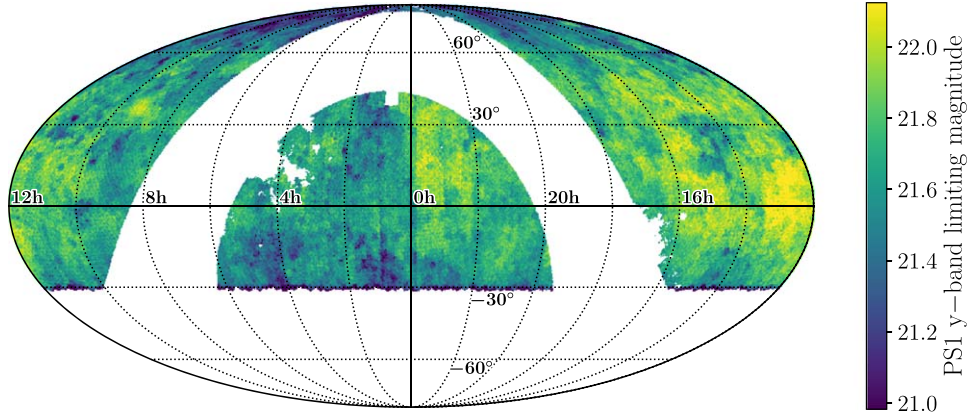


Figure 19. The PS1 y-band limiting magnitude for our quasar selection survey area. The figure details are analogous to those of Figure 3, but only for the PS1 y band.

Appendix D The PS1 Quasar Sample Data Table

We present the full PS1 quasar sample in Table 7 below. The columns show (1) the official PS1 designation; (2) the

dereddened PS1 y-band magnitudes; (3) the spectroscopic redshift; (4) the calculated absolute magnitude M_{1450} ; (5) the discovery references; and (6) the reference for the redshift measurement.




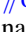





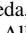
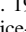
Table 7
Quasars and Their Properties Used in the PS1 QLF Analysis

PS1 Designation	y_{P1} (mag)	z	M_{1450} (mag)	References	z References
PSOJ157.61297+05.41528	19.86	6.31	-26.80	Fan et al. (2001a)	Kurk et al. (2007)
PSOJ245.88256+31.20014	20.25	6.26	-26.43	Fan et al. (2004)	Wang et al. (2011)
PSOJ162.18777+46.62181	19.67	6.23	-27.01	Fan et al. (2003)	Carilli et al. (2010)
PSOJ184.33893+01.52846	21.47	6.20	-25.19	Bañados et al. (2016), Wang et al. (2017)	Bañados et al. (2016)
PSOJ060.55290+24.85678	19.92	6.18	-26.74	Bañados et al. (2016)	Bañados et al. (2016)
PSOJ281.33614+53.76314	20.21	6.18	-26.44	Bañados et al. (2022)	Bañados et al. (2022)
PSOJ359.13521-06.38312	20.07	6.17	-26.59	Bañados et al. (2016), Wang et al. (2016b)	Eilers et al. (2021)
PSOJ242.40529+30.69660	20.46	6.16	-26.19	Jiang et al. (2016), S. J. Warren et al. (2022)	S. J. Warren et al. (2022)
PSOJ130.76568+29.18709	21.00	6.15	-25.64	Wang et al. (2019b)	Wang et al. (2019b)
PSOJ334.01815-05.00488	21.09	6.15	-25.56	Bañados et al. (2022)	Bañados et al. (2022)
PSOJ127.05586+26.56541	20.42	6.14	-26.22	Bañados et al. (2016), S. J. Warren et al. (2022)	Bañados et al. (2022)
PSOJ218.77147+04.81896	20.47	6.14	-26.18	Bañados et al. (2022)	Bañados et al. (2022)
PSOJ192.71635+31.50608	20.33	6.14	-26.30	Fan et al. (2006)	Shen et al. (2019)
PSOJ199.79708+09.84763	19.82	6.13	-26.82	Mortlock et al. (2009)	Venemans et al. (2020)
PSOJ065.50414-19.45796	20.27	6.12	-26.36	Bañados et al. (2016)	Decarli et al. (2018)
PSOJ160.32976+20.13997	20.66	6.12	-25.97	Wang et al. (2018)	Wang et al. (2019b)
PSOJ239.71246-07.40266	19.33	6.11	-27.30	Bañados et al. (2016)	Eilers et al. (2021)
PSOJ002.37869+32.87025	21.10	6.10	-25.52	Bañados et al. (2016)	Bañados et al. (2016)
PSOJ315.22789-17.25606	21.23	6.08	-25.39	Willott et al. (2010)	Venemans et al. (2020)
PSOJ240.72490+42.47359	19.82	6.08	-26.80	Fan et al. (2004)	Shen et al. (2019)
PSOJ130.62263+12.31404	19.86	6.08	-26.75	De Rosa et al. (2011), Jiang et al. (2015)	Decarli et al. (2018)
PSOJ239.78789+22.20398	20.88	6.07	-25.73	Wang et al. (2017)	Wang et al. (2017)
PSOJ247.64126+40.20269	20.62	6.06	-25.98	Fan et al. (2003)	Shen et al. (2019)
PSOJ293.03178+71.65233	20.11	6.05	-26.50	Bañados et al. (2016)	Bañados et al. (2016)
PSOJ250.34052+37.92226	21.09	6.05	-25.51	Willott et al. (2007)	Willott et al. (2010)
PSOJ210.72777+40.40088	21.00	6.04	-25.59	Bañados et al. (2016)	Bañados et al. (2016)
PSOJ313.52710-00.08733	20.57	6.04	-26.03	Jiang et al. (2008)	Venemans et al. (2020)
PSOJ181.90597+06.50283	20.15	6.04	-26.46	Jiang et al. (2015)	Decarli et al. (2018)
PSOJ196.53444+03.94065	20.07	6.03	-26.53	Fan et al. (2001a)	Venemans et al. (2020)
PSOJ265.92982+41.41395	21.32	6.03	-25.27	Bañados et al. (2022)	Eilers et al. (2020)
PSOJ124.61417+17.38111	19.26	6.02	-27.34	Fan et al. (2006)	Carilli et al. (2010)
PSOJ194.48949+63.82699	20.42	6.02	-26.18	Jiang et al. (2015)	Jiang et al. (2015)
PSOJ340.20404-18.66219	20.39	6.01	-26.21	Bañados et al. (2014)	Bañados et al. (2016)
PSOJ174.32386+35.83245	19.41	6.01	-27.18	Fan et al. (2006)	Shen et al. (2019)
PSOJ007.02733+04.95712	20.15	6.00	-26.43	Bañados et al. (2014), Jiang et al. (2015)	Venemans et al. (2020)
PSOJ037.97064-28.83892	20.58	6.00	-26.01	Bañados et al. (2014)	Bañados et al. (2016)
PSOJ182.31219+53.46335	21.05	5.99	-25.53	Bañados et al. (2022)	Bañados et al. (2022)
PSOJ029.51725-29.08868	19.37	5.98	-27.21	Bañados et al. (2016)	Bañados et al. (2022)
PSOJ027.15681+06.00556	19.35	5.98	-27.23	Jiang et al. (2015)	Becker et al. (2015b)
PSOJ056.71684-16.47693	20.07	5.97	-26.50	Bañados et al. (2016)	Eilers et al. (2020)
PSOJ288.64769+63.24792	20.76	5.96	-25.81	Bañados et al. (2022)	Bañados et al. (2022)
PSOJ130.33131+29.08460	20.19	5.95	-26.37	Goto (2006)	Shen et al. (2019)
PSOJ167.47265+56.95211	20.62	5.95	-25.95	Bañados et al. (2016)	Bañados et al. (2016)
PSOJ267.00210+22.78120	21.04	5.95	-25.52	Bañados et al. (2016)	Bañados et al. (2016)
PSOJ002.10738-06.43457	20.29	5.93	-26.26	Jiang et al. (2015), Bañados et al. (2016)	Bañados et al. (2016)
PSOJ076.23444-10.88780	20.61	5.93	-25.95	Bañados et al. (2022)	Bañados et al. (2022)
PSOJ139.61940+19.67919	20.71	5.92	-25.83	Wang et al. (2018)	Wang et al. (2018)
PSOJ213.36298-22.56173	19.89	5.92	-26.65	Bañados et al. (2014)	Bañados et al. (2016)
PSOJ228.68712+21.23882	20.60	5.92	-25.95	Bañados et al. (2016)	Bañados et al. (2016)
PSOJ328.73399-09.50762	20.46	5.92	-26.08	Bañados et al. (2016)	Bañados et al. (2016)
PSOJ135.87045-13.83368	21.01	5.91	-25.53	Bañados et al. (2016)	Bañados et al. (2016)
PSOJ194.12902+25.54761	21.07	5.91	-25.47	Bañados et al. (2016)	Bañados et al. (2016)
PSOJ218.39674+28.33067	20.45	5.91	-26.09	Bañados et al. (2022)	Bañados et al. (2022)
PSOJ212.79703+12.29368	20.10	5.90	-26.44	Fan et al. (2004)	Kurk et al. (2007)
PSOJ023.00711-02.26753	20.20	5.90	-26.35	Bañados et al. (2016)	Bañados et al. (2016)
PSOJ319.60403-10.93263	20.05	5.90	-26.49	Bañados et al. (2016)	Bañados et al. (2016)
PSOJ216.31805+32.90265	20.37	5.89	-26.16	Cool et al. (2006)	Carilli et al. (2010)
PSOJ042.66908-02.91745	20.02	5.89	-26.51	Bañados et al. (2016)	Bañados et al. (2016)
PSOJ187.30502+04.32436	21.09	5.89	-25.45	Bañados et al. (2014)	Bañados et al. (2014)
PSOJ075.93563-07.50613	20.13	5.88	-26.40	Bañados et al. (2016)	Bañados et al. (2016)
PSOJ157.90703-02.65990	20.26	5.88	-26.27	Bañados et al. (2016)	Bañados et al. (2016)
PSOJ210.82969+09.04750	20.33	5.88	-26.20	Jiang et al. (2015), Bañados et al. (2016)	Bañados et al. (2016)
PSOJ175.42940+71.32363	20.62	5.86	-25.90	Bañados et al. (2022)	Bañados et al. (2022)

Table 7
(Continued)

PS1 Designation	y_{P1} (mag)	z	M_{1450} (mag)	References	z References
PSOJ183.29919–12.76762	19.22	5.86	–27.30	Bañados et al. (2014)	Bañados et al. (2014)
PSOJ025.23764–11.68319	19.86	5.85	–26.65	Bañados et al. (2016)	Bañados et al. (2016)
PSOJ127.28174+03.06571	20.73	5.85	–25.78	Bañados et al. (2016)	Bañados et al. (2016)
PSOJ190.92005+25.48995	20.61	5.85	–25.90	Bañados et al. (2014), Jiang et al. (2016)	Jiang et al. (2016)
PSOJ219.04890+50.11865	20.20	5.85	–26.32	Fan et al. (2006)	Carilli et al. (2010)
PSOJ130.14626+56.40561	19.56	5.84	–26.95	Fan et al. (2006)	Wang et al. (2010)
PSOJ001.46807–00.11546	20.91	5.84	–25.59	Fan et al. (2004)	De Rosa et al. (2011)
PSOJ148.48293+69.18128	20.23	5.84	–26.28	Bañados et al. (2022)	Bañados et al. (2022)
PSOJ197.71978+25.53518	20.76	5.84	–25.74	Bañados et al. (2016)	Bañados et al. (2016)
PSOJ210.87224–12.00948	21.11	5.84	–25.40	Bañados et al. (2014)	Bañados et al. (2014)
PSOJ306.35128–04.82274	20.57	5.84	–25.94	Bañados et al. (2022)	Bañados et al. (2022)
PSOJ175.90977+38.14133	20.08	5.84	–26.43	Jiang et al. (2016)	Eilers et al. (2020)
PSOJ352.40341–15.33732	21.20	5.83	–25.30	Bañados et al. (2018a)	Rojas-Ruiz et al. (2021)
PSOJ212.29742–15.98660	20.89	5.83	–25.61	Bañados et al. (2016)	Bañados et al. (2016)
PSOJ122.72630+51.09447	19.86	5.82	–26.64	Jiang et al. (2016)	Bañados et al. (2016)
PSOJ235.94506+17.00789	20.20	5.82	–26.30	Bañados et al. (2016)	Bañados et al. (2016)
PSOJ236.29124+16.60886	20.83	5.82	–25.67	Bañados et al. (2016)	Bañados et al. (2016)
PSOJ000.66411+25.84303	19.42	5.82	–27.08	Fan et al. (2004)	Shen et al. (2019)
PSOJ129.18276+00.91479	19.03	5.81	–27.47	Fan et al. (2001a)	Kurk et al. (2007)
PSOJ174.79204–12.28454	20.23	5.81	–26.26	Bañados et al. (2016)	Bañados et al. (2016)
PSOJ238.85104–06.89765	20.63	5.81	–25.86	Bañados et al. (2016)	Bañados et al. (2016)
PSOJ357.82898+06.40193	21.37	5.81	–25.12	Bañados et al. (2016)	Bañados et al. (2016)
PSOJ017.06916–11.99193	20.66	5.80	–25.82	Bañados et al. (2022)	Bañados et al. (2022)
PSOJ124.00326+12.99894	21.05	5.80	–25.43	Bañados et al. (2022)	Bañados et al. (2022)
PSOJ193.39924–02.78203	21.10	5.80	–25.39	Bañados et al. (2022)	Bañados et al. (2022)
PSOJ307.76357–05.19589	20.95	5.80	–25.53	Bañados et al. (2022)	Bañados et al. (2022)
PSOJ308.48295–27.64850	19.90	5.80	–26.59	Bañados et al. (2016)	Bañados et al. (2016)
PSOJ021.42133–25.88228	19.71	5.79	–26.78	Bañados et al. (2016)	Bañados et al. (2016)
PSOJ161.13770–01.41721	19.32	5.78	–27.16	Fan et al. (2000)	Venemans et al. (2020)
PSOJ169.84022+01.21906	21.20	5.78	–25.27	Wang et al. (2018)	Wang et al. (2018)
PSOJ215.15142–16.04173	19.25	5.78	–27.23	Morganson et al. (2012)	J. Li et al. (2022, in preparation)
PSOJ236.46704+60.47332	19.13	5.78	–27.35	Wang et al. (2016a)	Wang et al. (2016a)
PSOJ243.64732+01.24579	19.96	5.78	–26.52	Yang et al. (2019)	Yang et al. (2019)
PSOJ000.04163–04.27391	20.46	5.77	–26.01	Bañados et al. (2022)	Bañados et al. (2022)
PSOJ172.17701+26.88666	20.73	5.77	–25.73	Bañados et al. (2016)	Bañados et al. (2016)
PSOJ187.10477–02.56090	20.83	5.77	–25.63	Bañados et al. (2016)	Bañados et al. (2016)
PSOJ209.38256–08.71714	21.25	5.77	–25.21	Bañados et al. (2022)	Bañados et al. (2022)
PSOJ351.30935+26.47995	19.42	5.77	–27.06	Wang et al. (2016a)	Wang et al. (2016a)
PSOJ249.46742+02.69955	19.37	5.76	–27.10	Wenzl et al. (2021)	Wenzl et al. (2021)
PSOJ261.12470+37.30605	20.49	5.76	–25.97	Bañados et al. (2022)	Bañados et al. (2022)
PSOJ072.58253–07.89183	20.96	5.75	–25.49	Bañados et al. (2022)	Bañados et al. (2022)
PSOJ156.44661+38.95732	20.13	5.75	–26.34	Bañados et al. (2022)	Bañados et al. (2022)
PSOJ201.92220+57.54400	20.56	5.74	–25.89	Bañados et al. (2016)	Bañados et al. (2016)
PSOJ271.44556+49.30671	20.59	5.74	–25.86	Bañados et al. (2022)	Bañados et al. (2022)
PSOJ169.14063+58.88944	20.44	5.73	–26.01	Bañados et al. (2022)	Bañados et al. (2022)
PSOJ320.87027–24.36041	20.37	5.73	–26.07	Bañados et al. (2016)	Bañados et al. (2016)
PSOJ030.88490+00.20813	20.41	5.72	–26.03	Venemans et al. (2007)	Mortlock et al. (2009)
PSOJ209.20588–26.70839	19.45	5.72	–26.99	Bañados et al. (2016)	Bañados et al. (2016)
PSOJ071.45075–02.33330	19.13	5.69	–27.30	Bañados et al. (2016)	Bañados et al. (2016)
PSOJ175.40916–20.26547	20.37	5.69	–26.05	Bañados et al. (2016)	Bañados et al. (2016)
PSOJ196.34762+15.38990	20.44	5.69	–25.98	Bañados et al. (2022)	Bañados et al. (2022)
PSOJ207.59836+37.80990	20.59	5.69	–25.82	Bañados et al. (2022), Gloudemans et al. (2022)	Bañados et al. (2022)
PSOJ004.81406–24.29917	19.41	5.68	–27.02	Bañados et al. (2016)	Bañados et al. (2016)
PSOJ038.19141–18.57350	20.47	5.68	–25.95	Bañados et al. (2022)	Bañados et al. (2022)
PSOJ040.01591+17.54581	20.88	5.68	–25.52	Bañados et al. (2016)	Bañados et al. (2016)
PSOJ055.42440–00.80355	20.18	5.68	–26.24	Bañados et al. (2015b)	Bañados et al. (2015a)
PSOJ178.37330+28.50753	19.86	5.68	–26.56	Bañados et al. (2022)	Bañados et al. (2022)
PSOJ245.06367–00.19786	21.21	5.68	–25.20	Bañados et al. (2016)	Bañados et al. (2016)
PSOJ197.86749+45.80408	20.75	5.66	–25.65	Bañados et al. (2022)	Bañados et al. (2022)
PSOJ002.54292+03.06321	20.93	5.64	–25.46	Bañados et al. (2022)	Bañados et al. (2022)
PSOJ224.65067+10.21379	19.84	5.60	–26.55	Bañados et al. (2022)	Bañados et al. (2022)
PSOJ330.28172+23.64389	20.49	5.83	–26.01	Bañados et al. (2022), Gloudemans et al. (2022)	Gloudemans et al. (2022)

ORCID iDs

Jan-Torge Schindler  <https://orcid.org/0000-0002-4544-8242>
 Eduardo Bañados  <https://orcid.org/0000-0002-2931-7824>
 Thomas Connor  <https://orcid.org/0000-0002-7898-7664>
 Roberto Decarli  <https://orcid.org/0000-0002-2662-8803>
 Xiaohui Fan  <https://orcid.org/0000-0003-3310-0131>
 Emanuele Paolo Farina  <https://orcid.org/0000-0002-6822-2254>
 Chiara Mazzucchelli  <https://orcid.org/0000-0002-5941-5214>
 Riccardo Nanni  <https://orcid.org/0000-0002-2579-4789>
 Hans-Walter Rix  <https://orcid.org/0000-0003-4996-9069>
 Daniel Stern  <https://orcid.org/0000-0003-2686-9241>
 Bram P. Venemans  <https://orcid.org/0000-0001-9024-8322>
 Fabian Walter  <https://orcid.org/0000-0003-4793-7880>

References

- Akiyama, M., He, W., Ikeda, H., et al. 2018, *PASJ*, **70**, S34
 Alam, S., Albareti, F. D., Allende Prieto, C., et al. 2015, *ApJS*, **219**, 12
 Avni, Y., & Bahcall, J. N. 1980, *ApJ*, **235**, 694
 Astropy Collaboration, Price-Whelan, A. M., Sipőcz, B. M., et al. 2018, *AJ*, **156**, 123
 Astropy Collaboration, Robitaille, T. P., Tollerud, E. J., et al. 2013, *A&A*, **558**, A33
 Baldwin, J. A. 1977, *ApJ*, **214**, 679
 Bañados, E., Carilli, C., Walter, F., et al. 2018a, *ApJL*, **861**, L14
 Bañados, E., Decarli, R., Walter, F., et al. 2015a, *ApJL*, **805**, L8
 Bañados, E., Schindler, J.-T., & Venemans, B. P. 2022, arXiv:2212.04452
 Bañados, E., Venemans, B. P., Decarli, R., et al. 2016, *ApJS*, **227**, 11
 Bañados, E., Venemans, B. P., Mazzucchelli, C., et al. 2018b, *Natur*, **553**, 473
 Bañados, E., Venemans, B. P., Morganson, E., et al. 2014, *AJ*, **148**, 14
 Bañados, E., Venemans, B. P., Morganson, E., et al. 2015b, *ApJ*, **804**, 118
 Becker, G. D., & Bolton, J. S. 2013, *MNRAS*, **436**, 1023
 Becker, G. D., Bolton, J. S., & Lidz, A. 2015a, *PASA*, **32**, e045
 Becker, G. D., Bolton, J. S., Madau, P., et al. 2015b, *MNRAS*, **447**, 3402
 Becker, G. D., D'Aloisio, A., Christenson, H. M., et al. 2021, *MNRAS*, **508**, 1853
 Bischetti, M., Feruglio, C., D'Odorico, V., et al. 2022, *Natur*, **605**, 244
 Boroson, T. A., & Green, R. F. 1992, *ApJS*, **80**, 109
 Bosman, S. E. I. 2021, arXiv:2108.12446
 Boutsia, K., Grazian, A., Calderone, G., et al. 2020, *ApJ*, **250**, 26
 Boutsia, K., Grazian, A., Fontanot, F., et al. 2021, *ApJ*, **912**, 111
 Boyle, B. J., Shanks, T., Croom, S. M., et al. 2000, *MNRAS*, **317**, 1014
 Boyle, B. J., Shanks, T., & Peterson, B. A. 1988, *MNRAS*, **235**, 935
 Calderone, G., Boutsia, K., Cristiani, S., et al. 2019, *ApJ*, **887**, 268
 Calverley, A. P., Becker, G. D., Haehnelt, M. G., & Bolton, J. S. 2011, *MNRAS*, **412**, 2543
 Cappelluti, N., Comastri, A., Fontana, A., et al. 2016, *ApJ*, **823**, 95
 Carilli, C. L., Wang, R., Fan, X., et al. 2010, *ApJ*, **714**, 834
 Chambers, K. C., Magnier, E. A., Metcalfe, N., et al. 2016, arXiv:1612.05560
 Cool, R. J., Kochanek, C. S., Eisenstein, D. J., et al. 2006, *AJ*, **132**, 823
 Croom, S. M., Richards, G. T., Shanks, T., et al. 2009, *MNRAS*, **399**, 1755
 D'Aloisio, A., McQuinn, M., Davies, F. B., & Furlanetto, S. R. 2018, *MNRAS*, **473**, 560
 Davies, F. B., Hennawi, J. F., Eilers, A.-C., & Lukić, Z. 2018, *ApJ*, **855**, 106
 De Rosa, G., Decarli, R., Walter, F., et al. 2011, *ApJ*, **739**, 56
 Decarli, R., Walter, F., Venemans, B. P., et al. 2018, *ApJ*, **854**, 97
 Di Matteo, T., Springel, V., & Hernquist, L. 2005, *Natur*, **433**, 604
 Diamond-Stanic, A. M., Fan, X., Brandt, W. N., et al. 2009, *ApJ*, **699**, 782
 Eilers, A.-C., Hennawi, J. F., Decarli, R., et al. 2020, *ApJ*, **900**, 37
 Eilers, A.-C., Hennawi, J. F., Decarli, R., et al. 2021, *ApJ*, **914**, 74
 Euclid Collaboration, Barnett, R., Warren, S. J., et al. 2019, *A&A*, **631**, A85
 Fan, X. 1999, *AJ*, **117**, 2528
 Fan, X., Hennawi, J. F., Richards, G. T., et al. 2004, *AJ*, **128**, 515
 Fan, X., Narayanan, V. K., Lupton, R. H., et al. 2001a, *AJ*, **122**, 2833
 Fan, X., Strauss, M. A., Richards, G. T., et al. 2006, *AJ*, **131**, 1203
 Fan, X., Strauss, M. A., Schneider, D. P., et al. 2001b, *AJ*, **121**, 54
 Fan, X., Strauss, M. A., Schneider, D. P., et al. 2003, *AJ*, **125**, 1649
 Fan, X., Wang, F., Yang, J., et al. 2019, *ApJL*, **870**, L11
 Fan, X., White, R. L., Davis, M., et al. 2000, *AJ*, **120**, 1167
 Faucher-Giguère, C.-A. 2020, *MNRAS*, **493**, 1614
 Faucher-Giguère, C.-A., Lidz, A., Hernquist, L., & Zaldarriaga, M. 2008, *ApJ*, **688**, 85
 Fontanot, F., Cristiani, S., Monaco, P., et al. 2007, *A&A*, **461**, 39
 Foreman-Mackey, D., Hogg, D. W., Lang, D., & Goodman, J. 2013, *PASP*, **125**, 306
 Gehrels, N. 1986, *ApJ*, **303**, 336
 Giallongo, E., Grazian, A., Fiore, F., et al. 2015, *A&A*, **578**, A83
 Giallongo, E., Grazian, A., Fiore, F., et al. 2019, *ApJ*, **884**, 19
 Glikman, E., Djorgovski, S. G., Stern, D., et al. 2011, *ApJL*, **728**, L26
 Gloudemans, A. J., Duncan, K. J., Saxena, A., et al. 2022, *A&A*, **668**, A27
 Górski, K. M., Hivon, E., Banday, A. J., et al. 2005, *ApJ*, **622**, 759
 Goto, T. 2006, *MNRAS*, **371**, 769
 Grazian, A., Giallongo, E., Boutsia, K., et al. 2022, *ApJ*, **924**, 62
 Grazian, A., Giallongo, E., Fiore, F., et al. 2020, *ApJ*, **897**, 94
 Haardt, F., & Madau, P. 1996, *ApJ*, **461**, 20
 Haardt, F., & Madau, P. 2012, *ApJ*, **746**, 125
 Harris, C. R., Jarrod Millman, K., van der Walt, S. J., et al. 2020, *Natur*, **585**, 357
 Hinton, S. R. 2016, *JOSS*, **1**, 00045
 Inayoshi, K., Visbal, E., & Haiman, Z. 2020, *ARA&A*, **58**, 27
 Jiang, L., Fan, X., Annis, J., et al. 2008, *AJ*, **135**, 1057
 Jiang, L., Fan, X., Hines, D. C., et al. 2006, *AJ*, **132**, 2127
 Jiang, L., McGreer, I. D., Fan, X., et al. 2015, *AJ*, **149**, 188
 Jiang, L., McGreer, I. D., Fan, X., et al. 2016, *ApJ*, **833**, 222
 Jiang, L., Ning, Y., Fan, X., et al. 2022, *NatAs*, **6**, 850
 Kaiser, N., Aussel, H., Burke, B. E., et al. 2002, *Proc. SPIE*, **4836**, 154
 Kaiser, N., Burgett, W., Chambers, K., et al. 2010, *Proc. SPIE*, **7733**, 77330E
 Kim, Y., Im, M., Jeon, Y., et al. 2015, *ApJL*, **813**, L35
 Kim, Y., Im, M., Jeon, Y., et al. 2020, *ApJ*, **904**, 111
 Kormendy, J., & Ho, L. C. 2013, *ARA&A*, **51**, 511
 Kulkarni, G., Worseck, G., & Hennawi, J. F. 2019, *MNRAS*, **488**, 1035
 Kurk, J. D., Walter, F., Fan, X., et al. 2007, *ApJ*, **669**, 32
 Lusso, E., Worseck, G., Hennawi, J. F., et al. 2015, *MNRAS*, **449**, 4204
 Lyke, B. W., Higley, A. N., McLane, J. N., et al. 2020, *ApJS*, **250**, 8
 Lyu, J., & Rieke, G. H. 2017, *ApJ*, **841**, 76
 Madau, P., & Haardt, F. 2015, *ApJL*, **813**, L8
 Madau, P., Haardt, F., & Rees, M. J. 1999, *ApJ*, **514**, 648
 Magnier, E. A., Chambers, K. C., Flewelling, H. A., et al. 2020a, *ApJS*, **251**, 3
 Magnier, E. A., Sweeney, W. E., Chambers, K. C., et al. 2020b, *ApJS*, **251**, 5
 Marshall, H. L., Tananbaum, H., Avni, Y., & Zamorani, G. 1983, *ApJ*, **269**, 35
 Matsuoka, Y., Onoue, M., Kashikawa, N., et al. 2016, *ApJ*, **828**, 26
 Matsuoka, Y., Strauss, M. A., Kashikawa, N., et al. 2018, *ApJ*, **869**, 150
 McGreer, I., Moustakas, J., & Schindler, J. 2021, simqso: Simulated Quasar Spectra Generator, Astrophysics Source Code Library, ascl:2106.008
 McGreer, I. D., Fan, X., Jiang, L., & Cai, Z. 2018, *AJ*, **155**, 131
 McGreer, I. D., Jiang, L., Fan, X., et al. 2013, *ApJ*, **768**, 105
 McKinney, W. 2010, in Proc. 9th Python in Science Conf., ed. S. van der Walt & J. Millman (Austin, TX: SciPy), 56
 Morganson, E., De Rosa, G., Decarli, R., et al. 2012, *AJ*, **143**, 142
 Mortlock, D. J., Patel, M., Warren, S. J., et al. 2009, *A&A*, **505**, 97
 Neeleman, M., Novak, M., Venemans, B. P., et al. 2021, *ApJ*, **911**, 141
 Newville, M., Stensitzki, T., Allen, D. B., & Ingargiola, A. 2014, LMFIT: Non-linear Least-square Minimization and Curve-Fitting for Python, v0.8.0, Zenodo, doi:10.5281/zenodo.11813
 Niida, M., Nagao, T., Ikeda, H., et al. 2020, *ApJ*, **904**, 89
 Onken, C. A., Wolf, C., Bian, F., et al. 2022, *MNRAS*, **511**, 572
 Pacucci, F., & Loeb, A. 2019, *ApJL*, **870**, L12
 Page, M. J., & Carrera, F. J. 2000, *MNRAS*, **311**, 433
 Pan, Z., Jiang, L., Fan, X., Wu, J., & Yang, J. 2022, *ApJ*, **928**, 172
 2020, pandas development team, T.pandas-dev/pandas: Pandas, v1.1.5, Zenodo, doi:10.5281/zenodo.3509134
 Pâris, I., Petitjean, P., Aubourg, É., et al. 2014, *A&A*, **563**, A54
 Pâris, I., Petitjean, P., Ross, N. P., et al. 2017, *A&A*, **597**, A79
 Parsa, S., Dunlop, J. S., & McLure, R. J. 2018, *MNRAS*, **474**, 2904
 Pei, Y. C. 1995, *ApJ*, **438**, 623
 Ricci, F., Marchesi, S., Shankar, F., La Franca, F., & Civano, F. 2017, *MNRAS*, **465**, 1915
 Richards, G. T., Strauss, M. A., Fan, X., et al. 2006, *AJ*, **131**, 2766
 Rix, H.-W., Hogg, D. W., Boubert, D., et al. 2021, *AJ*, **162**, 142
 Rojas-Ruiz, S., Bañados, E., Neeleman, M., et al. 2021, *ApJ*, **920**, 150
 Ross, N. P., McGreer, I. D., White, M., et al. 2013, *ApJ*, **773**, 14
 Scaramella, R., Amiaux, J., Mellier, Y., et al. 2022, *A&A*, **662**, A112
 Schindler, J.-T., Fan, X., McGreer, I. D., et al. 2018, *ApJ*, **863**, 144
 Schindler, J.-T., Fan, X., McGreer, I. D., et al. 2019, *ApJ*, **871**, 258
 Schlafly, E. F., & Finkbeiner, D. P. 2011, *ApJ*, **737**, 103

- Schlegel, D. J., Finkbeiner, D. P., & Davis, M. 1998, [ApJ](#), **500**, 525
- Schmidt, M. 1968, [ApJ](#), **151**, 393
- Schmidt, M., Schneider, D. P., & Gunn, J. E. 1995, [AJ](#), **110**, 68
- Schneider, D. P., Richards, G. T., Hall, P. B., et al. 2010, [AJ](#), **139**, 2360
- Selsing, J., Fynbo, J. P. U., Christensen, L., & Krogager, J.-K. 2016, [A&A](#), **585**, A87
- Shen, X., Hopkins, P. F., Faucher-Giguère, C.-A., et al. 2020, [MNRAS](#), **495**, 3252
- Shen, Y., & Kelly, B. C. 2012, [ApJ](#), **746**, 169
- Shen, Y., Wu, J., Jiang, L., et al. 2019, [ApJ](#), **873**, 35
- Shin, S., Im, M., Kim, Y., et al. 2020, [ApJ](#), **893**, 45
- Temple, M. J., Hewett, P. C., & Banerji, M. 2021, [MNRAS](#), **508**, 737
- Tsuzuki, Y., Kawara, K., Yoshii, Y., et al. 2006, [ApJ](#), **650**, 57
- van der Walt, S., Colbert, S. C., & Varoquaux, G. 2011, [CSE](#), **13**, 22
- Venemans, B. P., Findlay, J. R., Sutherland, W. J., et al. 2013, [ApJ](#), **779**, 24
- Venemans, B. P., McMahon, R. G., Warren, S. J., et al. 2007, [MNRAS](#), **376**, L76
- Venemans, B. P., Walter, F., Neeleman, M., et al. 2020, [ApJ](#), **904**, 130
- Verner, D. A., Ferland, G. J., Korista, K. T., & Yakovlev, D. G. 1996, [ApJ](#), **465**, 487
- Vestergaard, M., & Wilkes, B. J. 2001, [ApJS](#), **134**, 1
- Virtanen, P., Gommers, R., Oliphant, T. E., et al. 2020, [NatMe](#), **17**, 261
- Vito, F., Gilli, R., Vignali, C., et al. 2016, [MNRAS](#), **463**, 348
- Wang, F., Fan, X., Yang, J., et al. 2017, [ApJ](#), **839**, 27
- Wang, F., Wang, R., Fan, X., et al. 2019a, [ApJ](#), **880**, 2
- Wang, F., Wu, X.-B., Fan, X., et al. 2016a, [ApJ](#), **819**, 24
- Wang, F., Yang, J., Fan, X., et al. 2018, [ApJL](#), **869**, L9
- Wang, F., Yang, J., Fan, X., et al. 2019b, [ApJ](#), **884**, 30
- Wang, F., Yang, J., Fan, X., et al. 2021, [ApJL](#), **907**, L1
- Wang, R., Carilli, C. L., Neri, R., et al. 2010, [ApJ](#), **714**, 699
- Wang, R., Wagg, J., Carilli, C. L., et al. 2011, [AJ](#), **142**, 101
- Wang, R., Wu, X.-B., Neri, R., et al. 2016b, [ApJ](#), **830**, 53
- Weigel, A. K., Schawinski, K., Treister, E., et al. 2015, [MNRAS](#), **448**, 3167
- Wenzl, L., Schindler, J.-T., Fan, X., et al. 2021, [AJ](#), **162**, 72
- Willott, C. J., Delorme, P., Omont, A., et al. 2007, [AJ](#), **134**, 2435
- Willott, C. J., Delorme, P., Reylé, C., et al. 2010, [AJ](#), **139**, 906
- Wu, X.-B., Wang, F., Fan, X., et al. 2015, [Natur](#), **518**, 512
- Wyithe, J. S. B., & Bolton, J. S. 2011, [MNRAS](#), **412**, 1926
- Yang, J., Wang, F., Fan, X., et al. 2019, [ApJ](#), **871**, 199
- Yang, J., Wang, F., Fan, X., et al. 2020, [ApJL](#), **897**, L14
- Yang, J., Wang, F., Fan, X., et al. 2021, [ApJ](#), **923**, 262
- Yang, J., Wang, F., Wu, X.-B., et al. 2016, [ApJ](#), **829**, 33
- Yue, M., Fan, X., Yang, J., & Wang, F. 2022, [ApJ](#), **925**, 169
- Zonca, A., Singer, L., Lenz, D., et al. 2019, [JOSS](#), **4**, 1298
- Zuo, L., & Phinney, E. S. 1993, [ApJ](#), **418**, 28